

Histology-informed liver diffusion MRI: biophysical model design and demonstration in cancer immunotherapy

Francesco Grussu^{1*}, Kinga Bernatowicz¹, Marco Palombo^{2,3}, Irene Casanova-Salas¹, Ignasi Barba^{1,4}, Sara Simonetti¹, Garazi Serna¹, Athanasios Grigoriou^{1,5}, Anna Voronova^{1,5}, Valezka Garay⁶, Juan Francisco Corral^{7,8}, Marta Vidorreta⁹, Pablo García-Polo García¹⁰, Xavier Merino^{7,8}, Richard Mast^{7,8}, Núria Roson^{7,8}, Manuel Escobar^{7,8}, Maria Vieito¹¹, Rodrigo Toledo¹, Paolo Nuciforo¹, Joaquin Mateo¹¹, Elena Garralda¹¹, Raquel Perez-Lopez^{1*}

*Joint corresponding authors. Email: fgrussu@vhio.net (F.G.), rperez@vhio.net (R.P.L.)

¹ Vall d'Hebron Institute of Oncology (VHIO), Vall d'Hebron Barcelona Hospital Campus, Spain ² Cardiff University Brain Research Imaging Centre (CUBRIC), School of Psychology, Cardiff University, Cardiff, United Kingdom ³ School of Computer Science and Informatics, Cardiff University, Cardiff, UK ⁴ University of Vic - Central University of Catalonia (UVic-UCC), Vic, Spain ⁵ Department of Biomedicine, Faculty of Medicine and Health Sciences, University of Barcelona, Barcelona, Spain ⁶ PET/MR Unit, CETIR-ASCIREs, Barcelona, Spain ⁷ Department of Radiology, Hospital Universitari Vall d'Hebron, Barcelona, Spain ⁸ Institut de Diagnòstic per la Imatge (IDI), Barcelona, Spain ⁹ Siemens Healthineers, Madrid, Spain ¹⁰ GE HealthCare, Madrid, Spain ¹¹ Medical Oncology Service, Vall d'Hebron Barcelona Hospital Campus, Vall d'Hebron Institute of Oncology (VHIO), Spain

Abstract

Innovative diffusion Magnetic Resonance Imaging (dMRI) models enable *in vivo* mapping of biologically meaningful properties such as cell size, potential biomarkers in cancer. However, while cancers frequently spread to the liver, models tailored for liver applications and easy to deploy in the clinic are still sought. We tackle this unmet need by delivering a practical and clinically viable liver dMRI modelling framework. Through direct comparison of candidate dMRI approaches in mouse and cancer patients' data, we select a model of intra-cellular diffusion fitted to highly diffusion-weighted images, as it provides the strongest radiological-histological correlates. We demonstrate the potential application of the proposed model in cancer immunotherapy, stratifying the risk of progression based on baseline cell size and density measurements from dMRI. This result, heretofore unreported and not achievable with standard dMRI indices (e.g., apparent diffusion coefficient), suggests that our approach may become a useful tool for precision imaging in oncology.

37 Introduction

38 Routine clinical Magnetic Resonance Imaging (MRI) focusses on visualising macroscopic
39 anatomical features, as presence of tumours. Nonetheless, MRI also offers the possibility of
40 measuring biological properties within each pixel of a three-dimensional (3D) scan – known as
41 *voxel*. This approach, referred to as quantitative MRI (qMRI)¹, involves the acquisition of multiple
42 images, each featuring a different contrast, which are then analysed jointly with a mathematical
43 model. qMRI provides promising metrics, which could become quantitative biomarkers
44 complementing the qualitative assessment by the expert radiologist². Diffusion MRI (dMRI) is a
45 qMRI approach that sensitises the signal to water diffusion with magnetic field gradients^{1,3,4}. Since
46 diffusion in biological tissues is influenced by the microenvironment where diffusion takes place,
47 dMRI ultimately enables the indirect estimation of properties at the micrometric scale⁵, such as
48 the size of cells restricting water^{6,7}. dMRI bridges the gap between macroscopic and microscopic
49 imaging, and has found applications in brain⁵, spinal cord⁸, prostate⁶, breast⁹ imaging and beyond.

50 Innovative dMRI techniques are also urgently needed in abdominal imaging, as in liver MRI^{10,11}.
51 The liver is a frequent site for cancer metastatisation¹², and liver tumours are common targets for
52 treatment response assessment in oncology. However, current response criteria such as RECIST¹³
53 have limitations, in that they rely on MRI or computed tomography (CT) merely to measure tumour
54 size, without accounting for changes under therapy at the cellular level. Novel dMRI metrics could
55 enable the non-invasive characterisation of cancer microenvironments, shedding light on the
56 composition of tumours that cannot be biopsied. The new readouts could also provide information
57 on tumour heterogeneity, relevant in the development of treatment resistance^{14,15}, and could better
58 stratify patients eligible for treatments such as immunotherapy¹⁶, given the challenge of predicting
59 which patients can benefit from these innovative drugs¹⁷. This would be a major advancement in
60 oncology, as it may allow for personalised treatment planning, reductions in sample sizes in
61 clinical trials, and ultimately improve patient outcomes¹⁸.

62 The most recent biophysical dMRI techniques describe the non-vascular liver tissue signal as the
63 sum of contributions from intra-cellular and extra-cellular water^{19–21}. While these models provide
64 promising readouts²², their practical use in real-world settings is made unfeasible by i) the high
65 number of dMRI images (and hence long scan time) required to support model fitting, and by ii)
66 the requirement for specialised dMRI acquisitions²³, beyond default examinations available in the
67 scanner console. In this study we aim to tackle this unmet need by delivering a practical liver dMRI
68 signal model that is truly feasible in hospital settings, i.e., on 1.5T or 3T systems, with scan time
69 that does not exceed 15 minutes, and using vendor-provided dMRI sequences. With this objective
70 in mind, we embraced the latest “histology-informed” dMRI development paradigm, which is
71 based on informing signal model design with co-localised histology. The framework has shown
72 promise in delivering dMRI approaches with unprecedented fidelity to cytoarchitecture^{24,25},
73 maximising biological specificity²⁶.

74 In this article, we aimed to identify a practical mathematical model that maximises the agreement
75 of dMRI estimates of metrics such as cell size, to their underlying histological counterparts. We
76 analysed a rich data set of dMRI scans and hematoxylin and eosin (HE)-stained images from
77 excised mouse livers and patients' liver biopsies. We used these data to select the model
78 maximising radiological-histological correlations, corroborating results with computer
79 simulations. Afterwards, we demonstrated the clinical utility of the designed approach in one
80 exemplificatory task, assessing response to immunotherapy in patients suffering from advanced
81 solid tumours – an urgent, unmet need, given the lack of robust predictors of treatment response
82 for this class of drugs¹⁷. In summary, our study delivers a liver dMRI approach that offers metrics
83 with high fidelity to histopathology, and which is feasible in the clinic. The proposed method,
84 based on a single-compartment model of restricted, intra-cellular diffusion, fitted to highly
85 diffusion-weighted (DW) images, identified which patients progress faster from baseline dMRI
86 scans. These results, while exploratory and requiring further confirmation, suggest that our dMRI
87 framework could provide complementary information to standard-of-care imaging, and thus play
88 a key role in oncology research and practice.

89

90 Results

91 Overview: data set

92 Fig. 1 illustrates the data used in this study. We will refer to data obtained in fixed mouse livers as
93 *preclinical*, while to data obtained in cancer patients as *clinical*.

94

95 Preclinical data consists of pulsed gradient spin echo (PGSE) DW MRI scans of seven fixed mouse
96 livers, performed *ex vivo* on a 9.4T Bruker system. It also includes whole-organ HE-stained
97 sections, obtained at known radiographic position. We studied the livers of mice sacrificed as part
98 of xenograft model development in prostate cancer. Six had been implanted with biopsies of
99 prostate cancer patients, while one had not had any implantation. While the livers from the
100 implanted mice did not grow any tumours, they feature a variety of pathologies, with three unique
101 histopathological phenotypes (Fig. S1). The liver from the mouse with no implantation features
102 normal liver structures, and we will refer to it as *Control*. Of the six implanted cases, two also
103 show normal liver tissue, with normal representation of all hepatic structures. We will refer to
104 these cases as *PatNA1* and *PatNA2* (patient biopsy implantation, but normal appearing). Another case
105 exhibits generalised necrosis and diffuse acute and chronic inflammation surrounding necrotic
106 areas, with presence of occluded thrombotic vessels. This specimen will be identified as *Patnec*
107 (patient biopsy implantation, with necrosis). Finally, three specimens feature an immature,
108 lymphoproliferative process, with various degrees of infiltration of small, lymphoid, atypical cells
109 with abundant mitosis, which infiltrate portal vessels and sinusoidal capillaries, but without

110 producing tumours. These will be referred to as Pat_{inf1} to Pat_{inf3} (patient biopsy implantation, with
111 lymphoid cell infiltration).

112

113 We obtained clinical data on cancer patients suffering from advanced solid tumours, participating
114 in an ongoing imaging study at the Barcelona Vall d'Hebron Institute of Oncology (VHIO, Spain).
115 The study involves the acquisition of MRI data, alongside clinical and biological information, in
116 patients eligible for a phase I immunotherapy trial. We included data from 33 patients with liver
117 malignancies (mean/std of age: 62.91/12.34 year; 16 male, 17 female). dMRI was based on
118 diffusion-weighted (DW) echo planar imaging (EPI) scans performed on a 1.5T Siemens Avanto
119 system (Twice-Refocussed Spin Echo (TRSE) DW-EPI) and on a 3T GE SIGNA Pioneer system
120 (PGSE DW-EPI). We also obtained digitised HE-stained biopsies from one of the liver tumours.
121 Biopsies were available for 18 patients, and were collected after dMRI, but before
122 immunotherapy. Clinical outcome (progression-free survival (PFS)) was available for 30 patients,
123 who effectively entered the immunotherapy trial.

124

125 We used dMRI-histology data to design the dMRI signal model ($N = 25$) and dMRI-PFS data for
126 immunotherapy response assessment ($N = 30$).

127

128 **Overview: dMRI signal models**

129 We studied five dMRI biophysical models, accounting for restricted diffusion inside spherical cells
130 and hindered diffusion in the extra-cellular space^{6,19,22}. Models can be grouped into two families
131 (Fig. 2.A; see Material and Methods).

132 The first family is more general, in that it does not make any assumption on which is higher
133 between intra-/extra-cellular ADC (ADC_I and ADC_E from now on). It includes:

- 134 i. *Diff-in-exTD*: it accounts for restricted IC diffusion within spherical cells⁶, and hindered
135 diffusion in the extra-cellular space, with diffusion time dependence (TD)²⁷ in both intra-
136 /extra-cellular spaces²⁸. The diffusion time quantifies the time during which water
137 molecules can sense cellular barriers, before the MR image is acquired.
- 138 ii. *Diff-in-ex*: as previous model *Diff-in-exTD*, but neglecting TD in the extra-cellular space.
139 Popular techniques such as IMPULSED¹⁹ or VERDICT²⁰ are essentially implementations
140 of this model.

141 Conversely, the second family explicitly assumes that $ADC_E > ADC_I$, similarly to related dMRI
142 techniques (e.g., Restriction Spectrum Imaging²⁹; power-law axon radius mapping⁷). It includes:

- 143 i. *Diff-in-exTDFast*: equivalent to *Diff-in-exTD*, ensuring that $ADC_E > ADC_I$.
- 144 ii. *Diff-in-exFast*: equivalent to *Diff-in-ex*, ensuring that $ADC_E > ADC_I$.

145 iii. *Diff-in*: a model where it is hypothesised that due to fast, extra-cellular diffusion, the extra-
146 cellular signal is negligible, and the measured signal is dominated by intra-cellular water.

147

148 **Overview: dMRI metrics**

149 All models enable the estimation of *volume-weighted mean cell size* (vCS_{MRI} , expressed in μm)
150 and *intra-cellular signal fraction* (F_{MRI} , dimensionless), which can be combined into an apparent
151 *cell density per unit volume* ($CD_{MRI} = F_{MRI}/vCS_{MRI}^3$, expressed in cell mm^{-3})²⁰. For reference, we
152 benchmarked these metrics against routine ADC (in $\mu\text{m}^2 \text{ms}^{-1}$) and apparent diffusion excess
153 kurtosis K (dimensionless) from diffusion kurtosis imaging (DKI)³⁰, popular dMRI indices
154 sensitive to cancer cellularity, easy to compute from short acquisitions^{20,31}.

155

156 We processed HE-stained histological data with automatic cell detection³² to derive histological
157 counterparts of vCS_{MRI} and F_{MRI} at known radiographic location. The histological metrics were:
158 histological volume-weighted mean cell size (vCS_{histo} , in μm), intra-cellular area fraction (F_{histo} ,
159 dimensionless), and cell density per unit area (CD_{histo} , in cell mm^{-2}). We compared vCS_{histo} and
160 F_{histo} to vCS_{MRI} and F_{MRI} (Fig. 2B).

161

162 **A one-pool model of intra-cellular diffusion provides the most histologically meaningful** 163 **metrics**

164 Fig. 3A summarises the different dMRI models, while Fig. 3B reports values of the MRI-Histology
165 *Total Correlation Score* (TCS) for all models. TCS measures the overall correlation between
166 histological and radiological readouts of cell size and intra-cellular fraction, and is obtained by
167 summing Pearson's correlation coefficients between vCS_{MRI} and vCS_{histo} , and between F_{MRI} and
168 F_{histo} (see Materials and Methods). Higher TCS point towards stronger histological-radiological
169 correlation. Negative correlations reduce TCS, so they are penalised.

170

171 The bar plot in Fig. 3B highlights that dMRI models where $ADC_E > ADC_I$, shown in violet shades,
172 provide consistently higher TCS values than models that do not make such an assumption (orange
173 shades). We observe the highest TCS for model *Diff-in*. Note that Fig. 3 refers to TCS values
174 obtained by fitting dMRI models only to high b-value images, as this provided the highest TCS
175 figures. Fig. S2 reports TCS for model fitting performed to the whole set of diffusion images. In
176 this case, TCS is lower, but again, models where $ADC_E > ADC_I$ provide the highest TCS. In Fig.
177 S2, *Diff-in-exFast* provides the highest TCS, although this is lower than *Diff-in* TCS in Fig. 3.

178

179 Fig. S3 reports rankings according to additional criteria, namely: the *Histology Fidelity Criterion*
180 (HFC), measuring the sum of absolute errors in F and vCS estimation via dMRI, and the *Bayesian*

181 *Information Criterion* (BIC)³³. BIC is commonly used in dMRI model development^{34,35}; it
182 quantifies the overall model fitting quality (penalizing model complexity), but without accounting
183 for histological information. Lower HFC and lower BIC imply better model performance. Fig. S3
184 reports the number of times, in percentage terms, that a model provides the lowest HFC and BIC
185 across our $N = 25$ MRI-histology cases. Results essentially confirm rankings seen on TCS: models
186 hypothesising $ADC_E > ADC_I$ are selected more frequently than models that do not do, according
187 to HFC. The model *Diff-in* is the most selected model according to both BIC and HFC (fig. S3.B;
188 fitting to high b-value images). Fig. S4 splits HFC and BIC rankings depending on the MRI
189 scanner. In all cases, models with $ADC_E > ADC_I$ (*Diff-in*, *Diff-in-exFast*, *Diff-in-exFastTD*) are
190 selected more frequently than models *Diff-in-ex* and *Diff-in-ex-TD*. When fitting is performed only
191 on high b-value images, *Diff-in* is the most selected model according to both BIC and HFC.

192

193 **Computer simulations confirm model selection from MRI measurements**

194 We performed Monte Carlo computer simulations to corroborate the model selection performed
195 on *ex vivo* and *in vivo* dMRI data. The simulations consisted in generating synthetic dMRI signals
196 according to the three dMRI protocols used in this study. We synthesised signals for a substrate
197 made of packed spherical cells (Fig. S5), a common body dMRI tissue model^{6,19,22,23}, and then
198 performed model selection on the synthetic signals (see Materials and Methods). Supplementary
199 Tables S1, S2, and S3 report TCS, HFC and BIC rankings from simulated signals. Results confirm
200 that model *Diff-in* enables the best estimation of cell size and intra-cellular fraction in the vast
201 majorities of cases, thus confirming *ex vivo* and *in vivo* MRI results.

202

203 **Our proposed approach: a one-compartment model of intra-cellular diffusion, fitted to high** 204 **b-values**

205 In view of all rankings reported above, our recommended modelling approach is the *fitting a one-*
206 *compartment model of restricted, intra-cellular diffusion within spherical cells to high b-values*
207 *images* (≈ 1800 s/mm² *ex vivo*, ≈ 900 s/mm² *in vivo*) – referred to as model *Diff-in*.

208

209 **Cell size and density estimates from the proposed dMRI model correlate with histology**

210 We now report on the Pearson's correlation coefficient r between histology, *Diff-in* and DKI
211 metrics. We consider correlations to be weak, moderate, and strong when $|r| < 0.4$, $|r| \geq 0.4$ but
212 $|r| < 0.6$, and $|r| \geq 0.6$.

213

214 Table 1 shows that the correlation between *Diff-in* F_{MRI} (intra-cellular fraction), vCS_{MRI} (cell size
215 index) and CD_{MRI} (cell density) with their counterparts F_{histo} , vCS_{histo} and CD_{histo} are
216 respectively weak ($r = 0.19$ between F_{MRI} and F_{histo}), moderate ($r = 0.44$ between vCS_{MRI} and

217 vCS_{histo}) and strong ($r = 0.70$ between CD_{MRI} and CD_{histo}). The weak correlation between F_{MRI}
218 and F_{histo} can be explained, at least in part, with the fact that F_{MRI} is a signal fraction, rather than
219 an actual volume/area fraction (unlike F_{histo}), i.e., it is influenced by T2/T1 differences between
220 intra-cellular and residual extra-cellular signals³⁶. Moreover, F_{MRI} estimation can be biased by
221 unaccounted exchange between intra-/extra-cellular water^{21,37}, which is not accounted for in our
222 signal models. Conversely, the much higher correlations between vCS_{MRI} and vCS_{histo} and
223 between CD_{MRI} and CD_{histo} , point towards the biological specificity of vCS_{MRI} and CD_{MRI} .

224

225 Table 1 also reports correlation coefficients for dMRI ADC and kurtosis K . Both ADC and K
226 exhibit significant, moderate correlations with histological properties, i.e., negative/positive
227 correlation of ADC/ K with cell density CD_{histo} ($r = -0.47$ and 0.43 respectively) – a result entirely
228 consistent with previous studies^{38,39}. Significant correlations are also seen with F_{histo} ($r = 0.40$, p
229 $= 0.048$ between K and F_{histo}). These findings are in line with known literature: ADC and K are
230 sensitive to the underlying tissue microstructure, but they are also unspecific, being surrogate
231 metrics that conflate different histopathological characteristics into a single number.

232

233 Fig. S6 and Fig. S7 show Pearson's correlation coefficients for all possible pairs of metrics, in the
234 form of correlation matrices. Correlations among dMRI metrics are seen, as a strong negative
235 correlation between CD_{MRI} and vCS_{MRI} ($r = -0.84$ for model *Diff-in-exFast* fitted at high b-value).
236 This finding, which indicates that tighter cell packings per unit volume are achieved with smaller
237 cells, appears biophysically plausible, being mirrored by histological CD_{histo} and vCS_{histo} ($r = -$
238 0.88 between CD_{histo} and vCS_{histo}). Other weak-to-moderate correlations are seen, e.g.: between
239 K and vCS_{MRI} ($r = -0.47$) and K and CD_{MRI} ($r = 0.38$), which agree with the correlations observed
240 between K and histological vCS_{histo} ($r = -0.31$) and CD_{histo} ($r = 0.43$). In general, metrics from
241 dMRI models where $ADC_E > ADC_I$ show stronger correlations with their histological counterparts
242 than models *Diff-in-exTD* and *Diff-in-ex*. We observe the strongest dMRI-histology correlations
243 for model *Diff-in* fitted to high b-value images.

244

245 **Metrics from the proposed dMRI model reveal intra-/inter-tumour characteristics**

246 Fig. 4 shows maps from the proposed dMRI model *Diff-in* alongside histological metrics in 3
247 mouse livers, representative of the 3 phenotypes seen in our mouse data (*Control*, for normal liver
248 structures; *Patinfl*, for small cell infiltration; *Patnec*, for necrosis). Visually, we observe excellent
249 co-localisation between MRI slices and histology sections. The histological details reveal higher
250 cellularity in sample *Patinfl* compared to *Control*, due to packing of small cells in between larger
251 hepatocytes, or an alternation of areas with lower/ higher cell density in sample *Patnec*. These
252 qualitative trends are confirmed in the histological maps F_{histo} , vCS_{histo} , CD_{histo} , with values in
253 physiologically plausible ranges, as for example intra-cellular fractions around 0.75 and cell sizes

254 of the order of $20 \mu\text{m}^{40,41}$. Maps F_{MRI} , vCS_{MRI} and CD_{MRI} replicate the contrasts seeing in their
255 histological counterparts F_{histo} , vCS_{histo} and CD_{histo} . Fig. S8 shows standard dMRI metrics,
256 namely ADC and kurtosis excess K , in the same mouse livers. Visual trends highlight that the
257 higher cell density of sample *Patinfl* translated to remarkably reduced ADC and increased K
258 compared to the *Control*. Lastly, Fig. S9 shows F_{MRI} , vCS_{MRI} and CD_{MRI} maps from another model
259 (*Diff-in-exFast*). Fig. S10 instead shows maps of the other metrics provided by models *Diff-in-*
260 *exFast* and *Diff-in* (intrinsic cytosol diffusivity $D_{0,I}$ and asymptotic ADC_E , $D_{E,\infty}$). The figures
261 highlight that overall, spatial trends seen in maps from the selected model *Diff-in* agree with those
262 seen in *Diff-in-exFast*, but metrics from the latter appear noisier. Metrics $D_{0,I}$ and $D_{E,\infty}$ show
263 limited between-sample contrast, and are difficult to validate histologically.

264

265 Table S4 reports qualitative per-sample mean and standard deviation of all MRI and histology
266 metrics in mice. F_{MRI} slightly underestimates F_{histo} , while vCS_{MRI} slightly overestimates
267 vCS_{histo} . We speculate that the discrepancies may be due, at least in part, to unaccounted factors
268 such as variability in intrinsic cell shape/cytosol diffusivity⁴² or water exchange²¹, and by the
269 difficulty of relating accurately 2D histology to 3D MRI⁴³.

270

271 Fig. 5 shows F_{MRI} , vCS_{MRI} and CD_{MRI} maps in patients, alongside biopsies. Histopathological
272 assessment highlights the variety of characteristics that can coexist within advanced solid tumours,
273 e.g.: areas of fibrosis; localised areas of tightly packed cancer cells, surrounded by stromal fibres;
274 necrosis. dMRI F_{MRI} , vCS_{MRI} , CD_{MRI} show contrasts that are plausible with such histopathological
275 features. For example, in a breast cancer liver metastasis in Fig. 5, we observe a core of low intra-
276 cellular fraction F_{MRI} and low cell density CD_{MRI} , compatible with necrosis. In a HCC case instead,
277 we see areas of high F_{MRI} and high CD_{MRI} , surrounded by lower F_{MRI} and lower CD_{MRI} ,
278 potentially indicating the alternation of high cell densities with fibrotic tissue. Fig. S11 shows
279 routine dMRI ADC and K in the same tumours. Spatial trends are also compatible with the
280 histology, e.g., high ADC and low K are seen in the necrotic core of the breast cancer tumour.
281 Supplementary Fig. S12 shows F_{MRI} , vCS_{MRI} and CD_{MRI} from model *Diff-in-exFast*. Image
282 contrasts match visually those seen in the same metrics from model *Diff-in* (the proposed
283 approach), giving confidence of the overall robustness of the biophysical modelling framework.
284 Nevertheless, maps appear noisier. Fig. S13 shows intra-cellular cytosol diffusivity $D_{0,I}$
285 asymptotic ADC_E ($D_{E,\infty}$) in the same tumours. Their speckled appearance suggests that these
286 metrics are difficult to measure accurately *in vivo*^{19,44}.

287

288 **Metrics from the proposed dMRI model stratify the risk of cancer progression in**
289 **immunotherapy**

290 Finally, we demonstrate the potential utility of the proposed liver dMRI model in an
291 exemplificatory response assessment task. Fig. 6 reports on the PFS stratification based on *Diff-in*
292 metrics. Panels on the left report results from Kaplan-Meier analyses, log-rank tests and Cox
293 regressions performed after binarising dMRI metrics (higher/lower than the median of the cohort).
294 Panels on the right report results from Cox regressions assessing the continuous dependence of
295 PFS on *Diff-in* metrics. We detect a statistically significant dependence of the risk of progression
296 on baseline vCS_{MRI} (log-rank test: $p = 0.047$, Fig. 6C) and CD_{MRI} (log-rank test: $p = 0.035$, Fig.
297 6E). These differences correspond to statistically significant Hazard Ratios (HRs) from Cox
298 regression (HR = 0.47, $p = 0.050$ for binarised vCS_{MRI} ; HR = 2.36, $p = 0.043$ for binarised CD_{MRI}).
299 The risk of progression is about twice as high in patients whose baseline cell size vCS_{MRI} is smaller
300 than the median vCS_{MRI} , or whose cell density CD_{MRI} is higher than the median CD_{MRI} .
301 Importantly, we obtained similar results when vCS_{MRI} and CD_{MRI} were not binarised, but rather
302 used as continuous predictors in Cox regressions (right panels in Fig. 6). In this latter case, the HR
303 was statistically significant for vCS_{MRI} (HR = 0.65, $p = 0.034$, Fig. 6D), and it approached
304 statistical significance for CD_{MRI} (HR = 1.40, $p = 0.055$, Fig. 6F). These association are not
305 confounded by age, sex or baseline tumour volume (Supplementary Table S5; HR = 0.59, $p = 0.02$
306 for vCS_{MRI} ; HR = 1.65, $p = 0.01$ for CD_{MRI}).

307
308 Fig. 7 and supplementary Fig. S14, Fig. S15 and Fig. S16 report on response assessment based on
309 on all other dMRI metrics (routine ADC and K in Fig. 7; cytosol diffusivity $D_{0,I}$ for model *Diff-in*
310 in Fig. S14; vascular fraction f_V in Fig. S15; all metrics from model *Diff-in-exFast* in Fig. S16).
311 While the estimated HRs for metrics vCS_{MRI} , F_{MRI} and CD_{MRI} from dMRI model *Diff-in-exFast*
312 are in the same direction as those from model *Diff-in*, their association with the probability of
313 progression is weaker (HR = 1.53, $p = 0.05$ for CD_{MRI} ; Table S5). We do not detect any association
314 between baseline ADC and K and the probability of progression (Fig. 7 and Table S5).

315

316 Discussion

317 The latest liver dMRI models aim to disentangle intra-cellular and extra-cellular water
318 contributions to the total signal^{16,19,22,23}. This powerful approach enables the estimation of
319 innovative tissue property maps, but its clinical deployment is hampered by the high number of
320 unknown tissue parameters to estimate, which requires impractically long dMRI
321 acquisitions^{19,45,46}. With this challenge in mind, this paper delivers a practical implementation of a
322 two-compartment dMRI signal model, tailored for liver imaging, and truly feasible in the clinic.
323 Through histology-informed model selection, we design a compact dMRI framework consisting
324 of fitting a one-pool model of restricted intra-cellular diffusion to highly DW images. The
325 framework provides cell size and density estimates that correlate with histology, and which enable
326 the stratification of the risk of cancer progression under immunotherapy.

327

328 To find the optimal dMRI signal implementation, we analysed co-localised dMRI and histology
329 data (N = 25) from fixed mouse livers and from cancer patients. We compared 5 signal models,
330 each fitted according to two distinct strategies, and ranked them for their ability to estimate intra-
331 cellular fraction and cell size, as seen on histology. Rankings unequivocally suggest the highest
332 radiological-histological agreement is obtained by *fitting a single-compartment model of restricted*
333 *diffusion within spherical cells* – a model here referred to as *Diff-in* –, to images acquired with b-
334 values higher than approximately 900 s/mm² *in vivo* and 1800 s/mm² *ex vivo*. Interestingly, our
335 central result, confirmed by Monte Carlo computer simulations, points towards the fact that
336 simpler models of diffusion can provide the highest fidelity to the underlying histology, if deployed
337 in appropriate measurement regimes. In practice, our approach suggests that focussing on
338 measurement regimes where the signal is dominated by intra-cellular diffusion, may enable the
339 deployment of simpler models, which still suffice to capture salient microstructural features^{7,47-49}.
340 Notably, our model selection results are consistent with the fact recent estimates of the extra-
341 cellular liver ADC, as high as 2.5 μm²/ms¹⁹. Such a high ADC_E implies that the extra-cellular
342 signal would decay to roughly 5% or less of its non-DW value even for b-values of 1200 s/mm²
343 ($\exp(-b ADC_E) \approx 0.05$ for $b = 1200 \text{ s/mm}^2 = 1.2 \text{ ms}^{-1} \mu\text{m}^2$ and $ADC_E = 2.5 \mu\text{m}^2 \text{ ms}^{-1}$), justifying
344 the use of single-compartment model of intra-cellular diffusion^{7,44,50}.

345
346 Importantly, we conducted dMRI model selection using a variety of criteria, namely: TCS (overall
347 correlation between dMRI and histology), HFC (accuracy in histological property estimation via
348 dMRI), and BIC³⁵ (dMRI model quality of fit, penalising model complexity). In general, all criteria
349 point towards the same direction, with model *Diff-in* fitted to high b-value images being the top-
350 ranking model. We would also like to emphasise that while we used 15 *in vivo* dMRI scans for
351 both model design and for the clinical demonstration, the same liver dMRI model implementation
352 (i.e., fitting model *Diff-in* on high b-value images) would have been selected had we only looked
353 at the *ex vivo* mouse data or at *in silico* signals (Fig. S4, Tables S1 to S3). This fact gives confidence
354 on the robustness and generalisability of our model design. Another important observation is that
355 both TCS and HFC, which are histology-informed, suggest that models constraining the extra-
356 cellular ADC to be higher than the intra-cellular ADC, outperform models without such a
357 constraint. Such a better performance does not stand out as clearly when looking at BIC rankings
358 instead (e.g., Fig. S3.A, Fig. S4.A, Fig. S4.B, Fig. S4.C). This minor discrepancy can be
359 understood considering that a good fitting quality may not necessary imply accurate parameter
360 estimation in presence of noise^{26,44}. It also stresses the importance of informing dMRI modelling
361 with histology, for improved biological specificity.

362
363 After selecting a practical dMRI model implementation, we investigated its utility in an
364 exemplificatory response assessment task. Immunotherapy has shown promise in several
365 cancers¹⁶. However, only a small fraction of patients truly benefits from this class of drugs, and
366 their identification prior to treatment is extremely challenging¹⁷. With this in mind, we investigated

367 whether it is possible to stratify the probability of progression under immunotherapy given baseline
368 dMRI metrics within liver tumours ($N = 30$). Several, independent statistical tests consistently
369 point towards the fact that smaller baseline dMRI cell sizes and higher dMRI cell densities are
370 associated to faster cancer progression (shorter PFS). To our knowledge, this is the first time that
371 such advanced dMRI markers have been tested for patient stratification in immunotherapy *in vivo*.
372 The deleterious impact of higher cell density on PFS is in line with other studies focussing on
373 different treatments, where higher tumour cellularity has been associated with higher cancer
374 aggressiveness or worse prognosis. In CRC liver metastasis resection, for example, high cell
375 density in resected metastases has been associated to shorter disease-free survival⁵¹. Conversely,
376 in breast cancer, lower tumour cellularity has been associated to pathologic complete response in
377 chemo-free dual HER2 blockade treatment (for HER2-positive breast cancer)⁵², as well as longer
378 survivals in neoadjuvant chemotherapy⁵³. The significant association between PFS and dMRI cell
379 size/density reported here is promising, and motivates future studies to confirm it.

380

381 We benchmarked the proposed dMRI approach against well-established DKI apparent diffusion
382 and kurtosis coefficients (ADC and K)³⁰. ADC and K are easy to compute with compact dMRI
383 acquisitions, and are sensitive to cancer cellularity⁴⁶, a fact confirmed by our data. However, in
384 our cohort, neither of ADC and K showed statistically significant associations with clinical PFS.
385 This may due, at least partly, to the fact that ADC and K are semi-quantitative, protocol-dependent
386 metrics, whose value can change as function of factors as the diffusion time^{46,54}. Here, we did not
387 perform inter-scanner harmonisation deliberately, to stress the quantitative nature of our cell
388 size/density mapping approach, which inherently accounts for inter-scanner protocol differences.
389 However, it is possible that better performances for semi-quantitative ADC and K may be obtained
390 by adopting inter-scanner harmonisation⁵⁵.

391

392 We would like to acknowledge the following potential limitations. Firstly, our sample size ($N =$
393 25 for model development; $N = 30$ for the clinical demonstration) is relatively small. This paper
394 provides a first demonstration of the potential utility of the proposed *Diff-in* approach. The
395 demonstration is unique of its kind, since it reports heretofore undescribed dMRI-based
396 stratification in immunotherapy. Nonetheless, while works proposing related dMRI techniques
397 relied on similar^{23,36}, if not even smaller^{19,20}, sample sizes, we acknowledge that our exploratory
398 findings require further confirmation in larger cohorts.

399

400 Secondly, we point out that results from any dMRI-histology comparison should always be taken
401 with care. Here we related dMRI metrics obtained *in vivo* to histological indices from biopsies.
402 While we were able to identify the tumours from which the biopsies were taken, we could not
403 identify exactly the tumour area that was biopsied. This may imply that the biopsies are not fully
404 representative of the tumour microenvironment in its entirety. Also, and most importantly,

405 histology has its own limitations, since it provides cell property estimates that may not be, *per se*,
406 fully accurate. For example, routine HE histology is an inherently 2D technique, unlike 3D MRI.
407 Moreover, it is affected by artifacts (e.g., due to dehydration, paraffin embedding, imperfect
408 staining, cutting, etc⁵⁶), and the automatic processing of large fields-of-view requires trading off
409 between sensitivity and specificity. We took steps to mitigate these issues, e.g., by accounting for
410 biases due to tissue shrinkage. Nonetheless, our histology-derived estimates of cell properties are
411 likely biased versions of the true figures.

412

413 We would also like to acknowledge that the proposed dMRI approach neglects other potentially
414 relevant microstructural properties, such as water exchange between intra-/extra-cellular
415 spaces^{21,37}, presence of cell size/cytosolic diffusivity distributions^{42,57}, or intra-compartmental T2
416 or T1³⁶. On the one hand, ignoring these properties may have biased the estimation of F_{MRI} and
417 vCS_{MRI} ^{21,37}. On the other hand, properties such as exchange rates, overlooked in our model, may
418 be relevant markers of cellular stress *per se*. In future, we plan to incorporate these properties in
419 our models, while ensuring the clinical feasibility of the dMRI protocols required to fit them.

420

421 To conclude, *this study delivers a practical liver dMRI signal model consisting of a single-*
422 *compartment of restricted diffusion within spherical cells, which should be fitted to b-values higher*
423 *than, approximately, 900 s/mm² in vivo.* This model offers estimates of cell size and cell density
424 that are correlated to the underlying histology, and which may provide complementary information
425 to routine volumetric tumour burden assessment, for example by stratifying the risk of cancer
426 progression in immunotherapy. Striving to bringing precision imaging one step closer to the clinic,
427 we release our approach as an easy-to-use, open-source Python implementation, which will be
428 freely accessible online.

429

430 **Methods**

431 **dMRI models**

432 Common biophysical body dMRI signal models^{6,19,20,50,58,59} describe the signal as arising from
433 three, non-exchanging proton pools: vascular water; restricted, intra-cellular water; hindered,
434 extra-cellular, extra-vascular water. The dMRI signal for a PGSE measurement at b-value b ,
435 gradient duration/separation δ/Δ , and echo time TE is

436

$$437 \quad s = s_0 \left(f_V e^{-\frac{TE}{T_{2V}}} a_V + (1 - f_V) \left(f_I e^{-\frac{TE}{T_{2I}}} a_I + (1 - f_I) e^{-\frac{TE}{T_{2E}}} a_E \right) \right). \quad (1)$$

438

439 Above, s_0 is the apparent proton density, f_V is the voxel vascular signal fraction, f_I is the tissue
 440 intra-cellular signal fraction, $T2_V/T2_I/T2_E$ and $a_V/a_I/a_E$ are compartment-wise T2 and diffusion-
 441 weighting factors.

442 a_V captures intra-voxel incoherent motion (IVIM) effects⁶⁰. *In vivo*, the IVIM vascular ADC
 443 ranges approximately⁶¹ [15; 60] $\mu\text{m}^2 \text{ms}^{-1}$. For this reason, for $b > 100 \text{ s/mm}^2$, the vascular signal
 444 vanishes ($a_V \approx 0$), and Eq. (1) reduces to¹⁹

445

$$446 \quad s = s_0 (1 - f_V) \left(f_I e^{-\frac{TE}{T2_I}} a_I + (1 - f_I) e^{-\frac{TE}{T2_E}} a_E \right). \quad (2)$$

447

448 A common model for a_I in Eq. 2 is that of restricted diffusion within spheres of diameter L ^{19,20}:

449

$$450 \quad a_I = e^{-b \text{ADC}_I(\delta, \Delta, D_{0,I}, L)}, \quad (3)$$

451

452 where

453

$$454 \quad \text{ADC}_I = \frac{2}{D_{0,I} \delta^2 (\Delta - \delta/3)} \sum_{m=1}^{\infty} \frac{\alpha_m^{-4}}{\alpha_m^2 R^2 - 2} \left(2\delta - \frac{2 + e^{-\alpha_m^2 D_{0,I} (\Delta - \delta)} - 2e^{-\alpha_m^2 D_{0,I} \delta} - 2e^{-\alpha_m^2 D_{0,I} \Delta} + e^{-\alpha_m^2 D_{0,I} (\Delta + \delta)}}{\alpha_m^2 D_{0,I}} \right) \quad (4)$$

455

456

457 is the Gaussian phase distribution approximation of the intra-cellular ADC⁶². Above, α_m is the m -
 458 th root of $\alpha_m R J'_{3/2}(\alpha_m R) - 0.5 J_{3/2}(\alpha_m R) = 0$, $J_{3/2}(x)$ is the Bessel function of the first kind and order
 459 $3/2$, and $J'_{3/2}(x)$ its first-order derivative. ADC_I depends on the intrinsic cytosol diffusivity $D_{0,I}$ and
 460 on the cell size $L = 2R$ (R : radius; L : diameter). Noting that dMRI-derived L represents a volume-
 461 weighted mean cell size statistics^{7,42}, we will refer to it as *volume-weighted cell size (vCS)*.

462

463 Conversely, the extra-cellular, extra-vascular signal may be described in terms of hindered
 464 diffusion in a tortuous space^{19,27,59}:

465

$$466 \quad a_E(b, \Delta) = e^{-b \text{ADC}_E(\Delta, D_E, \infty, \beta)}, \quad (5)$$

467

468 with

469

$$470 \quad ADC_E(\Delta, D_{E,\infty}, \beta) = D_{E,\infty} + \frac{\beta}{\Delta}. \quad (6)$$

471

472 In Eq. 6, $D_{E,\infty}$ is the asymptotic⁵⁹ ADC_E for $\Delta \rightarrow \infty$.

473

474 The 5 implementations of the two-compartment model

475 We investigated 5 implementations of Eq. 2, divided into two families. The first family includes
476 models that do not make assumptions on which of ADC_I/ADC_E is higher:

- 477 i. *Diff-in-exTD*: the most general model, relying on the full expression of ADC_E in Eq. 6;
- 478 ii. *Diff-in-ex*: a simpler implementation of *Diff-in-exTD* that neglects extra-cellular TD ($\beta = 0$
479 in Eq. 6).

480 In the second family of models, we constrain $ADC_E > ADC_I$. It includes

- 481 i. *Diff-in-exTDFast*: equivalent to *Diff-in-exTD*, with the lower bound for $D_{E,\infty}$ ensuring
482 $ADC_E > ADC_I$ for any L .
- 483 ii. *Diff-in-exFast*: equivalent to *Diff-in-ex*, but again ensuring that $ADC_E > ADC_I$ for any L .
- 484 iii. *Diff-in*: a model where the extra-cellular signal is negligible compared to the intra-cellular
485 one, due to ADC_E being much larger than ADC_I , so that Eq. 2 simplifies to

486

$$487 \quad s = s_0 (1 - f_V) f_I e^{-\frac{TE}{T2_I}} a_I(b, \delta, \Delta, D_{0,I}, L). \quad (7)$$

488

489 In all models we used $T2_I \approx T2_E \doteq T2_T$, given the challenge of resolving accurately multiple T2
490 constants^{20,36}.

491

492 Fitting

493 We fitted the 5 models using custom-written Python routines, based on objective function
494 minimisation initialised by a grid search. The objective function was $f_{obj} = -\ln(\lambda)$, where λ is
495 the offset-Gaussian likelihood³⁴. Fitting provides estimates of vCS and voxel intra-cellular signal
496 fraction

497

$$498 \quad F = (1 - f_V) f_I. \quad (8)$$

499

500 We also combined vCS and F into a cell density per unit volume²⁰

501

$$502 \quad CD = \frac{F}{vCS^3}. \quad (9)$$

503

504 **Preclinical data**

505 Animals

506 We obtained data from 7 fixed livers of NOD.Cg-Prkdc^{scid} IL2rg^{tm1Wjl}/SzJ mice. All experimental
507 protocols were approved and monitored by the Vall d'Hebron Institute of Research Animal
508 Experimentation Ethics Committee (CEEA; registration number 68/20) in accordance with
509 relevant local and EU regulations. We studied six livers from mice implanted with cells derived
510 from biopsies of prostate cancer patients, as part of an ongoing study, plus an additional liver from
511 a mouse without any implantation. We implanted one tumor biopsy core with growth factor-
512 enriched Matrigel (Corning) subcutaneously in the flank of each mice. We derived tissue from the
513 following biopsies: iliac bone metastasis biopsy (metastatic castration-resistant prostate cancer,
514 presenting with bone metastasis and Gleason score 3+4 adenocarcinoma); prostate biopsy (patient
515 with metastatic hormone-sensitive prostate cancer, presenting with bone metastasis and Gleason
516 score 5+4 adenocarcinoma); two liver biopsies (patient with metastatic castration-resistant prostate
517 cancer, presenting with bone and visceral metastasis and Gleason score 4+4 acinar
518 adenocarcinoma; patient with metastatic hormone-sensitive prostate cancer, presenting with bone
519 and liver metastasis and Gleason score 4+4 adenocarcinoma). After implantation, we measured
520 tumour size using calipers and monitored mouse weight weekly, sacrificing animals by cervical
521 dislocation under general anesthesia when tumour volume exceeded 2000 mm³. We collected the
522 livers, fixed them overnight in formalin, and transferred them to phosphate-buffered saline (PBS)
523 solution.

524

525 MRI

526 We scanned livers on a 9.4T Bruker Avance system at room temperature. Livers were tightened
527 with sewing thread to a histology cassette and placed into a Falcon[®] tube, filled with PBS solution.
528 A 1-channel birdcage coil was used (excitation/reception). The protocol included a T2-weighted
529 fast spin echo sequence (resolution: 144 $\mu\text{m} \times 144 \mu\text{m} \times 2.216 \text{ mm}$) and PGSE dMRI (Fig. S17A;
530 TR = 2700 ms; resolution: 386 $\mu\text{m} \times 386 \mu\text{m}$; matrix size: 86 \times 86; 4 slices, 2.216 mm-thick, NEX
531 = 1). The protocol featured: $\delta = 10 \text{ ms}$, $\Delta = \{15, 30\} \text{ ms}$, 10 linearly spaced b-values for each Δ
532 (minimum/maximum nominal b: 0/2800 s/mm²). DW images corresponding to $\Delta = 15 \text{ ms}$ were
533 acquired at each of TE = {31, 45, 65} ms, and to $\Delta = 30 \text{ ms}$ at each of TE = {45, 65} ms. We i)
534 denoised dMRI scans with Marchenko-Pastur Principal Component Analysis (MP-PCA) Python
535 denoising⁶³ (kernel: 7 \times 7 \times 3), ii) mitigated Gibbs ringing (MrTrix3 local sub-voxel shift method⁶⁴),

536 and iii) corrected temporal signal drifts by assessing signal changes in a PBS solution region,
537 accounting for TE (PBS T2: 500 ms).

538 Finally, we fitted the *Diff-in-exTD*, *Diff-in-exTDFast*, *Diff-in-ex*, *Diff-in-exFast* and *Diff-in* models
539 voxel-by voxel (tissue parameter bounds: [0; 1] for f_I ; [0.8; 2.6] $\mu\text{m}^2 \text{ms}^{-1}$ for $D_{0,I}$; [8; 40] μm for
540 vCS ; [0.8; 2.6] $\mu\text{m}^2 \text{ms}^{-1}$ for $D_{E,\infty}$ in models *Diff-in-ex* and *Diff-in-exTD* and [1.75; 2.6] $\mu\text{m}^2 \text{ms}^{-1}$
541 in models *Diff-in-exFast* and *Diff-in-exTDFast*; [0; 10] μm^2 for β in models *Diff-in-ex-TD* and
542 *Diff-in-exTDFast*). For fitting, we fixed f_V and $T2_T$ to values obtained through a two-pool
543 vascular-tissue model⁶⁵ (fitting bounds: [0; 1] for f_V ; [5; 80] ms for $T2_T$). Fitting was performed
544 i) on all images with $b > 1000 \text{ s/mm}^2$ (suppressing vascular signals, referred to as *fitting on whole*
545 *image set*); ii) on $b > 1000 \text{ s/mm}^2$ images (*high b-value fitting*). In our *ex vivo* data, the vascular
546 signal captures PBS solution contamination (PBS ADC: roughly $2.4 \mu\text{m}^2 \text{ms}^{-1}$). For this reason,
547 we adopted a b-value threshold of 1000 s/mm^2 to achieve acceptable PBS signal suppression. We
548 used instead a minimum b-value of 1800 s/mm^2 for high b-value fitting (minimising extra-cellular
549 contributions), given the reduction in intrinsic tissue diffusivity expected *ex vivo*.

550

551 For comparison, we computed ADC and apparent diffusion excess kurtosis K by fitting

552

$$553 \quad s = s_0 e^{-b \text{ADC} + \frac{1}{6}K(b \text{ADC})^2} \quad (10)$$

554

555 to DW images acquired at $TE = 45 \text{ ms}$, $\Delta = 30 \text{ ms}$, with in-house Python code.

556

557 Histology

558 After MRI, samples underwent histology. We cut two $4 \mu\text{m}$ -thick histological sections at known
559 position, stained them with HE, and digitised them (Hamamatsu C9600-12 slide scanner; 0.227
560 μm resolution). An experienced pathologist (S.S.) inspected images qualitatively. We then
561 processed them with the automatic cell detection tool of QuPath³², obtaining per-cell area A and
562 diameter $l = \sqrt{\frac{4}{\pi}A}$. Afterwards, we split images into $386 \mu\text{m} \times 386 \mu\text{m}$ patches (matching the MRI
563 resolution), computing patch-wise histological volume-weighted cell size vCS_{histo} , intra-cellular
564 area fraction F_{histo} and cell density per unit area CD_{histo} ⁴². vCS_{histo} , defined as

565

$$566 \quad vCS_{histo} = \left(\frac{\langle l^7 \rangle}{\langle l^3 \rangle} \right)^{\frac{1}{4}}, \quad (11)$$

567

568 is a more accurate counterpart of dMRI cell size than the arithmetic mean^{7,42} $aCS_{histo} = \langle l \rangle$.
569 We accounted for biases coming from: i) estimating the size of 3D objects from 2D views (bias
570 1), ii) tissue shrinkage (bias 2), by rescaling vCS_{histo} and CD_{histo} . The final vCS_{histo} estimate was
571 1.4616 times larger than the value obtained from direct image processing ($1.4616 = 1.2732 \times 1.148$;
572 1.2732, derived from the theory of spherical caps, accounts for bias 1; 1.148 accounts for bias 2,
573 and corresponds to a plausible shrinkage of 12.9% following dehydration, clearing and paraffin
574 embedding⁵⁶). The final CD_{histo} estimate was 1.318 times smaller than the value derived from
575 direct image processing, since 1 mm² of shrunk tissue corresponds to 1.148×1.148 mm² = 1.318
576 mm² of unprocessed tissue (plausible shrinkage 12.9%⁵⁶). Lastly, we co-registered histological
577 maps to MRI⁴² using DiPy⁶⁶.

578

579 **Clinical data**

580 Cohort

581 We obtained data from patients suffering from advanced solid tumours, recruited for an ongoing
582 imaging study approved by the Vall d'Hebron University Hospital Ethics committee
583 (PR(AG)29/2020). Patients, eligible for a phase I immunotherapy trial at VHIO (Barcelona,
584 Spain), provided informed written consent to participate in the imaging study. We included 33
585 patients with liver malignancies (mean/std of age: 62.91/12.34 year; 16 male, 17 female), of which
586 3 suffered from primary HCC, while 30 had liver metastases from different primary cancers (10
587 colon, 8 melanoma, 3 rectal, 2 ovarian, 2 gastric, 2 breast, 1 renal, 1 endometrial, 1 ureteral). We
588 obtained baseline dMRI scans (i.e., acquired immediately before starting immunotherapy), and
589 digitised HE-stained biopsies from one of the imaged liver tumours. We obtained biopsies from
590 18 patients (6 scanned at 1.5T, 12 at 3T), collected after baseline dMRI. 30 out of 33 patients
591 finally entered the immunotherapy trial after screening; for them, a clinical outcome in the form
592 of PFS was available. PFS represents the lag between therapy starting date and progression or
593 death (whichever occurs first), with progression determined via RECIST¹³, or in case of
594 established clinical worsening.

595

596 MRI

597 We imaged patients at the level of the abdomen. We scanned 11 patients on a 1.5T Siemens Avanto
598 scanner using the vendor 18-channel body coil for detection. The protocol included a T2-weighted
599 fast spin echo scan (resolution: $1.4 \times 1.4 \times 5$ mm³; 32 slices; TR = 4500 ms; TE = 82 ms; echo
600 train length: 29; NEX = 8; GRAPPA = 2) and fat-suppressed DW TRSE (Fig. S17B) EPI (dMRI
601 scan time: 16 minutes). It featured: resolution: $1.9 \times 1.9 \times 6$ mm³; 32 slices; TR = 7900 ms;
602 bandwidth 1430 Hz/pixel; averaging of 3 orthogonal diffusion directions \times 2 signal averages
603 (effective NEX = 6); GRAPPA factor of 2; 6/8 partial Fourier imaging. The dMRI protocol
604 consisted of $b = \{0, 50, 100, 400, 900, 1200, 1600\}$ s/mm², each for TE = $\{93, 105, 120\}$ ms. One
605 additional image ($b = 0$ s/mm²; TE = 93 ms) was acquired with reversed phase encoding polarity.

606 The gradient timings (Fig. S17B) were: $\delta_1 = 8.9$ ms, $\delta_2 = 17.6$ ms, $\delta_3 = 20.4$ ms, $\delta_4 = 6.0$ ms, $\Delta_{1,2}$
607 $= 17.4$ ms and $\Delta_{1,4} = 63.9$ ms when TE = 93 ms; $\delta_1 = 13.2$ ms, $\delta_2 = 19.3$ ms, $\delta_3 = 24.8$ ms, $\delta_4 = 7.7$
608 ms, $\Delta_{1,2} = 21.7$ ms and $\Delta_{1,4} = 74.2$ ms when TE = 105 ms; $\delta_1 = 18.9$ ms, $\delta_2 = 21.0$ ms, $\delta_3 = 30.5$
609 ms, $\delta_4 = 9.5$ ms, $\Delta_{1,2} = 27.5$ ms and $\Delta_{1,4} = 87.5$ ms when TE = 120 ms. The b-value is

610

$$611 \quad b = \gamma^2 G^2 \left(\delta_1^2 (\Delta_{1,2} - \delta_1) + \frac{2}{3} (\delta_1 + \delta_2)^3 + (\delta_1 + \delta_2 - \delta_3)^2 (\Delta_{1,4} - \Delta_{1,2} - \delta_2 - \delta_3) \right). \quad (12)$$

612

613 We scanned 22 more patients on a 3T GE SIGNA Pioneer scanner, using the vendor 48-channel
614 torso coil for signal reception, with 32 channels enabled for detection. The protocol included a
615 respiratory-gated T2-weighted fast spin echo scan (resolution: $1.4 \times 1.4 \times 6$ mm³; 32 slices; TR =
616 4615 ms; TE = 52.86 ms; echo train length: 16) and respiratory-gated, fat-suppressed PGSE (Fig.
617 S10A) EPI (dMRI scan time: 16 minutes). It featured: resolution: $2.4 \times 2.4 \times 6$ mm³; 32 slices; TR
618 = 6000 ms; bandwidth 1953 Hz/pixel; averaging of 3 orthogonal diffusion directions \times 2 signal
619 averages (effective NEX = 6); ASSET factor of 2. The dMRI protocol consisted of $b = \{0, 50, 100,$
620 $400, 900, 1200, 1500\}$ s/mm², each for TE = $\{75, 90, 105\}$ ms. The gradient timings (Fig. S17A)
621 were: gradient duration $\delta = \{0.0, 3.9, 5.2, 9.2, 15.0, 18.2, 21.0\}$ ms for TE = 75 ms, $\delta = \{0.0, 3.9,$
622 $5.2, 9.2, 13.0, 15.8, 18.5\}$ ms for TE = 90 ms and 105 ms; gradient separation $\Delta = \{0.0, 27.8, 29.0,$
623 $33.0, 28.7, 31.8, 34.7\}$ ms for TE = 75 ms and $\Delta = \{0.0, 27.8, 29.0, 33.0, 37.0, 39.6, 42.3\}$ ms for
624 TE = 90 ms and TE = 105 ms.

625

626 dMRI post-processing consisted of slice-wise Python MP-PCA denoising (kernel: 5×5)⁶³;
627 MRTrix3 Gibbs unringing⁶⁴; motion correction via affine co-registration⁶⁷; FSL distortion
628 correction⁶⁸ (1.5T data only). An experienced radiologists (R.P.L.) segmented tumours on the T2-
629 w scan, enabling per-patient tumour volume computation. Afterwards, we warped the tumour mask
630 to dMRI using ANTs⁶⁹ non-linear co-registration, and fitted the 5 dMRI models, fixing again f_V
631 and $T2_T$ to previously computed values⁶⁵ (fitting bounds: $[0; 1]$ for f_V ; $[20; 140]$ ms for $T2_T$; $[0;$
632 $1]$ for f_I ; $[0.8; 3.0]$ $\mu\text{m}^2 \text{ms}^{-1}$ for $D_{0,I}$; $[8; 40]$ μm for vCS ; $[0.8; 3.0]$ $\mu\text{m}^2 \text{ms}^{-1}$ for $D_{E,\infty}$ in models
633 *Diff-in-ex* and *Diff-in-exTD*, and $[1.75; 3.0]$ $\mu\text{m}^2 \text{ms}^{-1}$ in models *Diff-in-exFast* and *Diff-in-*
634 *exTDFast*; $[0; 10]$ μm^2 for β in models *Diff-in-ex-TD* and *Diff-in-exTDFast*).

635

636 We fitted the 5 dMRI models i) on images acquired at a b-value $b > 100$ s/mm², to suppress
637 vascular signals (*fitting to the whole image set*); ii) to $b > 900$ s/mm² images, to also minimize
638 extra-cellular contributions (*high b-value fitting*). For scans performed on the 1.5T Siemens
639 system: i) we used $\Delta_{1,2} + \delta_2$ in place of Δ in Eq. 6 (Fig. S10B), ii) we replaced Eq. 4 with a
640 numerical implementation of restricted diffusion within spheres, based on Radial Basis Function
641 interpolation of synthetic signals generated for DW-TRSE with Monte Carlo simulations⁷⁰.

642

643 For both scanners, we also computed ADC and excess kurtosis K by fitting Eq. 10 on $b > 100$
644 s/mm^2 images (shortest TE), with in-house Python code.

645

646 Histology

647 We performed ultrasound-guided biopsies of one liver tumour at the Barcelona Vall d'Hebron
648 University Hospital (Spain). The biological material underwent standard processing, HE staining
649 and digitalisation (Hamamatsu C9600-12 slide scanner; resolution: $0.454 \mu\text{m}$). An experienced
650 pathologist (S.S.) assessed the images and drew a region-of-interest (ROI) outlining the tumours.
651 In parallel, an experienced radiologist (R.P.L.) inspected ultrasound and MR images, outlining the
652 biopsied tumour on the latter. We processed HE data with QuPath and computed per-biopsy
653 vCS_{histo} , F_{histo} and CD_{histo} , as previously described. Finally, we rescaled vCS_{histo} and CD_{histo} ,
654 by multiplying vCS_{histo} from image processing by 1.503 ($1.503 = 1.1806 \times 1.2732$, where 1.2732
655 accounts for biases from 2D sectioning, and 1.1806 accounts for a plausible tissue shrinkage of
656 15.3% following fixation, dehydration, clearing and paraffin embedding⁵⁶). The final CD_{histo}
657 estimate was instead 1.3938 times smaller than the value derived from direct image processing,
658 since 1 mm^2 of shrunk tissue corresponds to $1.1806 \times 1.1806 \text{ mm}^2 = 1.3938 \text{ mm}^2$ of unprocessed
659 tissue for a shrinkage factor of 15.3%⁵⁶.

660

661 **Statistical analyses**

662 *dMRI model selection*

663 We carried out model selection independently for each of the two fitting strategies. The MRI-
664 histology *Total Correlation Score* (TCS) selects the model providing the highest Pearson's
665 correlation between vCS_{MRI} and vCS_{histo} , and between F_{MRI} and F_{histo} . It is defined as

666

$$667 \text{TCS} = r(vCS_{MRI}, vCS_{histo}) + r(F_{MRI}, F_{histo}), (13)$$

668

669 where $r(vCS_{MRI}, vCS_{histo})$ and $r(F_{MRI}, F_{histo})$ are the correlation coefficients of vCS_{MRI} and
670 F_{MRI} with histological vCS_{histo} and F_{histo} . The correlation between CD_{MRI} and CD_{histo} was not
671 included in Eq. 13 since CD_{MRI} is determined analytically from vCS_{MRI} and F_{MRI} . For TCS
672 computation, we pooled together mouse and human data ($N = 25$).

673

674 We also performed model selection using a *Histology Fidelity Criterion* (HFC), and popular
675 *Bayesian Information Criterion* (BIC)^{33,34}. HFC rewards the models providing the best accuracy

676 in the numerical estimation of histological cell size and intra-cellular fraction estimation, i.e.,
677 minimising

678

$$679 \quad \text{HFC} = \frac{|vCS_{MRI} - vCS_{histo}|}{vCS_{histo}} + \frac{|F_{MRI} - F_{histo}|}{F_{histo}}. \quad (14)$$

680

681 Information on CD_{MRI} and CD_{histo} was not included in Eq. 14 since CD_{MRI} is not a degree of
682 freedom of the dMRI models (it is determined analytically from vCS_{MRI} and F_{MRI}). BIC selects
683 the model providing the best goodness of fit, penalising complexity, by minimising

684

$$685 \quad \text{BIC} = P \ln(N) - \ln(\lambda). \quad (15)$$

686

687 λ is the maximised likelihood, and P/N are the number of model parameters/signal measurements.
688 We performed BIC selection voxel-wise, followed by majority voting across voxels.

689

690 Simulated dMRI model selection

691 We synthesised signals via Monte Carlo diffusion random walks for each of the three dMRI
692 protocols of this study, using the MCDC simulator⁷⁰. We seeded walkers in a substrate made of
693 spherical cells of identical diameter^{6,19,22,23} (Fig. S5), controlling the intra-sphere fraction F by
694 adding gaps of increasing size in-between abutting spheres, packed in an ideal cubic lattice. We
695 probed four F values (0.197, 0.323, 0.406, 0.523) and four sphere diameters for each F (8, 16, 22
696 and 30 μm). We varied intra-/extra-sphere diffusivities (10×10 values; $[0.8; 2.6] \mu\text{m}^2 \text{ms}^{-1}$ for the
697 *ex vivo* protocol and $[0.8; 3.0] \mu\text{m}^2 \text{ms}^{-1}$ for *in vivo* protocols), for a total of 1600 synthetic voxels.
698 We corrupted synthetic signals with Rician noise ($b = 0$ signal-to-noise ratio: 30), and performed
699 model selection according to TCS, HFC and BIC.

700

701 dMRI-histology correlation analysis

702 We computed mean and standard deviation of all metrics i) within the mouse liver samples, ii)
703 within a mask containing all liver tumours in patients, iii) within the biopsied patients' tumours.
704 We pooled together metrics from mice and patients to calculate Pearson's correlation coefficients
705 r . In doing so, ADC was normalised to the ADC of the PBS solutions in mice and to the free water
706 diffusivity in patients ($3.0 \mu\text{m}^2 \text{ms}^{-1}$ at 37 °C), given the difference in temperature.

707

708 Response assessment in immunotherapy

709 We studied mean values of *in vivo* baseline dMRI metrics within liver tumours to assess whether
710 these could stratify the probability of progression under immunotherapy, measured by PFS (N =
711 30). Firstly, we performed the stratification after binarising all MRI metrics as lower/higher than
712 the median of the cohort, creating two groups. We evaluated group-wise survival curves with the
713 Kaplan-Meier estimator, and compared them with a log-rank test. We also fitted a proportional
714 hazard Cox regression, where the binarised MRI metric was the only regressor. Secondly, we
715 stratified PFS without binarising MRI metrics. We fitted a proportional hazard Cox model using
716 each continuous dMRI metric as the only regressor (in the form of a z-score), and then fitted the
717 statistical model again, including age, sex and total baseline tumour volume as confounding
718 factors. We performed all analyses in Python, using *lifelines*.

719

720 **Acknowledgments**

721 We thank the whole medical oncology, radiology, pathology, molecular biology, clinical trial, and
722 IT teams at the Vall d’Hebron University Hospital and at the Vall d’Hebron Institute of Oncology
723 in Barcelona (Spain), without whom this study would not have been possible. We are also thankful
724 to the Vall d’Hebron Radiology department and to the ASCIRES CETIR clinical team for their
725 assistance, and to past and present members of the Radiomics group for useful discussion and
726 advice. Finally, we would like to express our sincere gratitude to all patients and their families for
727 dedicating their time to research. VHIO would like to acknowledge: the State Agency for Research
728 (Agencia Estatal de Investigación) for the financial support as a Center of Excellence Severo
729 Ochoa (CEX2020-001024-S/AEI/10.13039/501100011033), the Cellex Foundation for providing
730 research facilities and equipment and the CERCA Programme from the Generalitat de Catalunya
731 for their support on this research. This research has been supported by PREDICT, sponsored by
732 AstraZeneca. This study has been co-funded by the European Regional Development
733 Fund/European Social Fund 'A way to make Europe' (to R.P.L.), and by the Comprehensive
734 Program of Cancer Immunotherapy & Immunology (CAIMI), funded by the Banco Bilbao
735 Vizcaya Argentaria Foundation Foundation (FBBVA, grant 89/2017). R.P.L is supported by the
736 “la Caixa” Foundation CaixaResearch Advanced Oncology Research Program, the Prostate
737 Cancer Foundation (18YOUN19), a CRIS Foundation Talent Award (TALENT19-05), the FERO
738 Foundation through the XVIII Fero Fellowship for Oncological Research, the Instituto de Salud
739 Carlos III-Investigación en Salud (PI18/01395 and PI21/01019), the Asociación Española Contra
740 el Cancer (AECC) (PRYCO211023SERR) and the Generitat de Catalunya Agency for
741 Management of University and Research Grants of Catalonia (AGAUR) (2023PROD00178). The
742 project that gave rise to these results received the support of a fellowship from “la Caixa”
743 Foundation (ID 100010434). The fellowship code is “LCF/BQ/PR22/11920010” (funding F.G.,
744 A.V., and A.G.) and “LCF/BQ/PI20/11760033” (funding I.C.S). I.C.S. also receives the support
745 of the European Union’s Horizon 2020 research and innovation programme under the Marie
746 Sklodowska-Curie grant agreement No 847648. This research has received support from the
747 Beatriu de Pinós Postdoctoral Program from the Secretariat of Universities and Research of the

748 Department of Business and Knowledge of the Government of Catalonia, and the support from the
749 Marie Sklodowska-Curie COFUND program (BP3, contract number 801370; reference 2019 BP
750 00182) of the H2020 program (to K.B.). M.P. is supported by the UKRI Future Leaders Fellowship
751 MR/T020296/2. A.G. is supported by a Severo Ochoa PhD fellowship (PRE2022-102586).

752

753 **Author information**

754 Francesco Grussu and Raquel Perez-Lopez are joint corresponding authors.

755

756 **Authors and affiliations**

757 *Vall d'Hebron Institute of Oncology (VHIO), Vall d'Hebron Barcelona Hospital Campus,*
758 *Barcelona, Spain.* Francesco Grussu, Kinga Bernatowicz, Irene Casanova-Salas, Ignasi Barba,
759 Sara Simonetti, Garazi Serna, Athanasios Grigoriou, Anna Voronova, Rodrigo Toledo, Paolo
760 Nuciforo & Raquel Perez-Lopez.

761 *Cardiff University, Cardiff, United Kingdom.* Marco Palombo.

762 *University of Vic - Central University of Catalonia (UVic-UCC), Vic, Spain.* Ignasi Barba.

763 *Department of Biomedicine, Faculty of Medicine and Health Sciences, University of Barcelona,*
764 *Barcelona, Spain.* Athanasios Grigoriou & Anna Voronova.

765 *PET/MR Unit, CETIR-ASCIREs, Barcelona, Spain.* Valezka Garay.

766 *Department of Radiology, Hospital Universitari Vall d'Hebron, Barcelona, Spain.* Juan Francisco
767 Corral, Xavier Merino, Richard Mast, Núria Roson & Manuel Escobar.

768 *Institut de Diagnòstic per la Imatge (IDI), Barcelona, Spain.* Juan Francisco Corral, Xavier
769 Merino, Richard Mast, Núria Roson & Manuel Escobar.

770 *Siemens Healthineers, Madrid, Spain.* Marta Vidorreta.

771 *GE HealthCare, Madrid, Spain.* Pablo García-Polo García.

772 *Medical Oncology Service, Vall d'Hebron Barcelona Hospital Campus, Vall d'Hebron Institute*
773 *of Oncology (VHIO), Barcelona, Spain.* Maria Vieito, Joaquin Mateo & Elena Garralda

774

775 **Contributions**

776 Conceptualization: F.G., R.P.L., K.B., M.P., E.G., R.T., P.N., J.M. Methodology: F.G., R.P.L.,
777 K.B., M.P., A.G. Investigation: F.G., R.P.L., K.B., I.C.S., I.B., S.S., G.S., A.G., V.G., J.F.C., X.M.,
778 R.M., N.R., M.E., M.Vie., R.T., P.N., J.M., E.G. Resources: R.P.L., F.G., P.N., J.M., E.G., N.R.,
779 M.E., V.G., M.Vid., P.G.P.G, I.B. Formal analysis: F.G. Visualization: F.G. Software: F.G., K.B.,
780 A.G. Data curation: F.G., R.P.L., K.B., A.V., G.S., I.C.S., A.G. Project administration: F.G.,
781 R.P.L., K.B., E.G., P.N., R.T., J.M., I.C.S. Funding acquisition: R.P.L., E.G., R.T., P.N., J.M.,

782 F.G., K.B., I.C.S. Supervision: F.G., R.P.L., E.G., R.T., P.N., J.M. Writing—original draft: F.G.,
783 R.P.L., K.B., M.P. Writing—review & editing: all authors

784 **Corresponding authors**

785 Correspondence to Francesco Grussu or Raquel Perez-Lopez.

786

787 **Ethics declarations**

788 **Competing interests**

789 This study received funding from AstraZeneca. M.Vid. works for Siemens Healthineers. P.G.P.G.
790 works for GE HealthCare. K.B. worked as a researcher at the Vall d’Hebron Institute of Oncology
791 (Barcelona), and is now an employee of AstraZeneca. AstraZeneca, Siemens and General Electric
792 did not influence the acquisition and analysis of the data, the interpretation of the results, or the
793 decision to submit the manuscript in its current form for publication.

794 **Ethics**

795 All experimental protocols in animals were approved and monitored by the Vall d’Hebron Institute
796 of Research Animal Experimentation Ethics Committee (CEEA; registration number 68/20) in
797 accordance with relevant local and EU regulations. The imaging study in cancer patients was
798 approved by the Vall d’Hebron University Hospital Ethics committee (PR(AG)29/2020),
799 Barcelona, Spain. Patients provided informed written consent to participate in the study.

800

801 **Supplementary Information**

802 This article includes Supplementary Figure S1 to S17 and Supplementary Tables S1 to S5.

803

804 **References**

805

- 806 1. Weiskopf, N., Edwards, L. J., Helms, G., Mohammadi, S. & Kirilina, E. Quantitative magnetic
807 resonance imaging of brain anatomy and in vivo histology. *Nature Reviews Physics* **3**, 570–588
808 (2021).
- 809 2. Jarrett, A. M. *et al.* Quantitative magnetic resonance imaging and tumor forecasting of breast cancer
810 patients in the community setting. *Nat. Protoc.* **16**, 5309–5338 (2021).
- 811 3. Kiselev, V. G. Fundamentals of diffusion MRI physics. *NMR Biomed.* **30**, (2017).
- 812 4. Novikov, D. S., Fieremans, E., Jespersen, S. N. & Kiselev, V. G. Quantifying brain microstructure
813 with diffusion MRI: Theory and parameter estimation. *NMR Biomed.* **32**, e3998 (2019).
- 814 5. Le Bihan, D. Looking into the functional architecture of the brain with diffusion MRI. *Nat. Rev.*
815 *Neurosci.* **4**, 469–480 (2003).
- 816 6. Panagiotaki, E. *et al.* Noninvasive quantification of solid tumor microstructure using VERDICT
817 MRI. *Cancer Res.* **74**, 1902–1912 (2014).

- 818 7. Veraart, J. *et al.* Noninvasive quantification of axon radii using diffusion MRI. *Elife* **9**, e49855
819 (2020).
- 820 8. Cohen-Adad, J. *et al.* Generic acquisition protocol for quantitative MRI of the spinal cord. *Nat.*
821 *Protoc.* **16**, 4611–4632 (2021).
- 822 9. Baxter, G. C., Graves, M. J., Gilbert, F. J. & Patterson, A. J. A Meta-analysis of the Diagnostic
823 Performance of Diffusion MRI for Breast Lesion Characterization. *Radiology* **291**, 632–641 (2019).
- 824 10. Donato, H., França, M., Candelária, I. & Caseiro-Alves, F. Liver MRI: From basic protocol to
825 advanced techniques. *Eur. J. Radiol.* **93**, 30–39 (2017).
- 826 11. Tapper, E. B. & Lok, A. S.-F. Use of Liver Imaging and Biopsy in Clinical Practice. *N. Engl. J.*
827 *Med.* **377**, 756–768 (2017).
- 828 12. Tsilimigras, D. I. *et al.* Liver metastases. *Nat Rev Dis Primers* **7**, 27 (2021).
- 829 13. Eisenhauer, E. A. *et al.* New response evaluation criteria in solid tumours: revised RECIST
830 guideline (version 1.1). *Eur. J. Cancer* **45**, 228–247 (2009).
- 831 14. Buikhuisen, J. Y., Torang, A. & Medema, J. P. Exploring and modelling colon cancer inter-tumour
832 heterogeneity: opportunities and challenges. *Oncogenesis* **9**, 66 (2020).
- 833 15. Vitale, I., Shema, E., Loi, S. & Galluzzi, L. Intratumoral heterogeneity in cancer progression and
834 response to immunotherapy. *Nat. Med.* **27**, 212–224 (2021).
- 835 16. Waldman, A. D., Fritz, J. M. & Lenardo, M. J. A guide to cancer immunotherapy: from T cell basic
836 science to clinical practice. *Nat. Rev. Immunol.* **20**, 651–668 (2020).
- 837 17. Pilard, C. *et al.* Cancer immunotherapy: it's time to better predict patients' response. *Br. J. Cancer*
838 **125**, 927–938 (2021).
- 839 18. O'Connor, J. P. B. *et al.* Imaging biomarker roadmap for cancer studies. *Nat. Rev. Clin. Oncol.* **14**,
840 169–186 (2017).
- 841 19. Jiang, X., Xu, J. & Gore, J. C. Mapping hepatocyte size in vivo using temporal diffusion
842 spectroscopy MRI. *Magn. Reson. Med.* **84**, 2671–2683 (2020).
- 843 20. Panagiotaki, E. *et al.* Microstructural Characterization of Normal and Malignant Human Prostate
844 Tissue With Vascular, Extracellular, and Restricted Diffusion for Cytometry in Tumours Magnetic
845 Resonance Imaging. *Invest. Radiol.* **50**, 218 (2015).
- 846 21. Gardier, R. *et al.* Cellular Exchange Imaging (CEXI): Evaluation of a diffusion model including
847 water exchange in cells using numerical phantoms of permeable spheres. *Magn. Reson. Med.* (2023)
848 doi:10.1002/mrm.29720.
- 849 22. Hoffmann, E. *et al.* Profiling specific cell populations within the inflammatory tumor
850 microenvironment by oscillating-gradient diffusion-weighted MRI. *J Immunother Cancer* **11**,
851 e006092 (2023).
- 852 23. Jiang, X. *et al.* MRI of tumor T cell infiltration in response to checkpoint inhibitor therapy. *J*
853 *Immunother Cancer* **8**, (2020).
- 854 24. Ye, Z. *et al.* Diffusion Histology Imaging Combining Diffusion Basis Spectrum Imaging (DBSI)
855 and Machine Learning Improves Detection and Classification of Glioblastoma Pathology. *Clin.*
856 *Cancer Res.* **26**, 5388–5399 (2020).

- 857 25. Howard, A. F. *et al.* Joint modelling of diffusion MRI and microscopy. *Neuroimage* **201**, 116014
858 (2019).
- 859 26. Novikov, D. S., Kiselev, V. G. & Jespersen, S. N. On modeling. *Magn. Reson. Med.* **79**, 3172–3193
860 (2018).
- 861 27. Xu, J. *et al.* Diffusion time dependency of extracellular diffusion. *Magn. Reson. Med.* **89**, 2432–
862 2440 (2023).
- 863 28. Neuman, C. H. Spin echo of spins diffusing in a bounded medium. *J. Chem. Phys.* **60**, 4508–4511
864 (1974).
- 865 29. Conlin, C. C. *et al.* Improved Characterization of Diffusion in Normal and Cancerous Prostate
866 Tissue Through Optimization of Multicompartmental Signal Models. *J. Magn. Reson. Imaging* **53**,
867 628–639 (2021).
- 868 30. Jensen, J. H., Helpert, J. A., Ramani, A. & Lu, H. Diffusional kurtosis imaging: the quantification
869 of non-gaussian water diffusion by means of magnetic resonance imaging. *in Medicine: An ...*
870 (2005).
- 871 31. Hectors, S. J. *et al.* Advanced Diffusion-weighted Imaging Modeling for Prostate Cancer
872 Characterization: Correlation with Quantitative Histopathologic Tumor Tissue Composition-A
873 Hypothesis-generating Study. *Radiology* **286**, 918–928 (2018).
- 874 32. Bankhead, P. *et al.* QuPath: Open source software for digital pathology image analysis. *Sci. Rep.* **7**,
875 16878 (2017).
- 876 33. Schwarz, G. Estimating the Dimension of a Model. *aos* **6**, 461–464 (1978).
- 877 34. Panagiotaki, E. *et al.* Compartment models of the diffusion MR signal in brain white matter: a
878 taxonomy and comparison. *Neuroimage* **59**, 2241–2254 (2012).
- 879 35. Ferizi, U. *et al.* A ranking of diffusion MRI compartment models with in vivo human brain data.
880 *Magn. Reson. Med.* **72**, 1785–1792 (2014).
- 881 36. Palombo, M. *et al.* Joint estimation of relaxation and diffusion tissue parameters for prostate cancer
882 with relaxation-VERDICT MRI. *Sci. Rep.* **13**, 2999 (2023).
- 883 37. Jiang, X., Devan, S. P., Xie, J., Gore, J. C. & Xu, J. Improving MR cell size imaging by inclusion of
884 transcytolemmal water exchange. *NMR Biomed.* **35**, e4799 (2022).
- 885 38. Rosenkrantz, A. B. *et al.* Assessment of hepatocellular carcinoma using apparent diffusion
886 coefficient and diffusion kurtosis indices: preliminary experience in fresh liver explants. *Magn.*
887 *Reson. Imaging* **30**, 1534–1540 (2012).
- 888 39. Tang, W.-J. *et al.* Evaluation of the Effects of Anti-PD-1 Therapy on Triple-Negative Breast Cancer
889 in Mice by Diffusion Kurtosis Imaging and Dynamic Contrast-Enhanced Imaging. *J. Magn. Reson.*
890 *Imaging* **56**, 1912–1923 (2022).
- 891 40. Martin, N. C. *et al.* Functional analysis of mouse hepatocytes differing in DNA content: volume,
892 receptor expression, and effect of IFN γ . *J. Cell. Physiol.* **191**, 138–144 (2002).
- 893 41. Zhou, Z., Xu, M.-J. & Gao, B. Hepatocytes: a key cell type for innate immunity. *Cell. Mol.*
894 *Immunol.* **13**, 301–315 (2016).

- 895 42. Grussu, F. *et al.* Diffusion MRI signal cumulants and hepatocyte microstructure at fixed diffusion
896 time: Insights from simulations, 9.4T imaging, and histology. *Magn. Reson. Med.* (2022)
897 doi:10.1002/mrm.29174.
- 898 43. Morawski, M. *et al.* Developing 3D microscopy with CLARITY on human brain tissue: Towards a
899 tool for informing and validating MRI-based histology. *Neuroimage* **182**, 417–428 (2018).
- 900 44. Jelescu, I. O., Veraart, J., Fieremans, E. & Novikov, D. S. Degeneracy in model parameter
901 estimation for multi-compartmental diffusion in neuronal tissue. *NMR Biomed.* **29**, 33–47 (2016).
- 902 45. Nilsson, M. *et al.* Mapping prostatic microscopic anisotropy using linear and spherical b-tensor
903 encoding: A preliminary study. *Magn. Reson. Med.* **86**, 2025–2033 (2021).
- 904 46. Fokkinga, E. *et al.* Advanced Diffusion-Weighted MRI for Cancer Microstructure Assessment in
905 Body Imaging, and Its Relationship With Histology. *J. Magn. Reson. Imaging* (2023)
906 doi:10.1002/jmri.29144.
- 907 47. Jensen, J. H., Russell Glenn, G. & Helpert, J. A. Fiber ball imaging. *Neuroimage* **124**, 824–833
908 (2016).
- 909 48. McKinnon, E. T., Helpert, J. A. & Jensen, J. H. Modeling white matter microstructure with fiber
910 ball imaging. *Neuroimage* **176**, 11–21 (2018).
- 911 49. Warner, W. *et al.* Temporal Diffusion Ratio (TDR) for imaging restricted diffusion: Optimisation
912 and pre-clinical demonstration. *Neuroimage* **269**, 119930 (2023).
- 913 50. Reynaud, O. Time-Dependent Diffusion MRI in Cancer: Tissue Modeling and Applications.
914 *Frontiers in Physics* **5**, (2017).
- 915 51. Serrablo, A. *et al.* Impact of novel histopathological factors on the outcomes of liver surgery for
916 colorectal cancer metastases. *Eur. J. Surg. Oncol.* **42**, 1268–1277 (2016).
- 917 52. Nuciforo, P. *et al.* A predictive model of pathologic response based on tumor cellularity and tumor-
918 infiltrating lymphocytes (CelTIL) in HER2-positive breast cancer treated with chemo-free dual
919 HER2 blockade. *Ann. Oncol.* **29**, 170–177 (2018).
- 920 53. Gentile, D. *et al.* Pathologic response and residual tumor cellularity after neo-adjuvant
921 chemotherapy predict prognosis in breast cancer patients. *Breast* **69**, 323–329 (2023).
- 922 54. Lee, H.-H., Papaioannou, A., Novikov, D. S. & Fieremans, E. In vivo observation and biophysical
923 interpretation of time-dependent diffusion in human cortical gray matter. *Neuroimage* **222**, 117054
924 (2020).
- 925 55. Fortin, J.-P. *et al.* Harmonization of multi-site diffusion tensor imaging data. *Neuroimage* **161**, 149–
926 170 (2017).
- 927 56. Boonstra, H., Oosterhuis, J. W., Oosterhuis, A. M. & Fleuren, G. J. Cervical tissue shrinkage by
928 formaldehyde fixation, paraffin wax embedding, section cutting and mounting. *Virchows Arch. A*
929 *Pathol. Anat. Histopathol.* **402**, 195–201 (1983).
- 930 57. Xu, J. *et al.* MRI-cytometry: Mapping nonparametric cell size distributions using diffusion MRI.
931 *Magn. Reson. Med.* **85**, 748–761 (2021).
- 932 58. Xu, J. *et al.* Magnetic resonance imaging of mean cell size in human breast tumors. *Magn. Reson.*
933 *Med.* **83**, 2002–2014 (2020).

- 934 59. Reynaud, O. *et al.* Pulsed and oscillating gradient MRI for assessment of cell size and extracellular
935 space (POMACE) in mouse gliomas. *NMR Biomed.* **29**, 1350–1363 (2016).
- 936 60. Le Bihan, D. *et al.* MR imaging of intravoxel incoherent motions: application to diffusion and
937 perfusion in neurologic disorders. *Radiology* **161**, 401–407 (1986).
- 938 61. Li, Y. T. *et al.* Liver intravoxel incoherent motion (IVIM) magnetic resonance imaging: a
939 comprehensive review of published data on normal values and applications for fibrosis and tumor
940 evaluation. *Quant. Imaging Med. Surg.* **7**, 59–78 (2017).
- 941 62. Balinov, B., Jonsson, B., Linse, P. & Soderman, O. The NMR Self-Diffusion Method Applied to
942 Restricted Diffusion. Simulation of Echo Attenuation from Molecules in Spheres and between
943 Planes. *J. Magn. Reson. A* **104**, 17–25 (1993).
- 944 63. Veraart, J. *et al.* Denoising of diffusion MRI using random matrix theory. *Neuroimage* **142**, 394–
945 406 (2016).
- 946 64. Kellner, E., Dhital, B., Kiselev, V. G. & Reiser, M. Gibbs-ringing artifact removal based on local
947 subvoxel-shifts. *Magn. Reson. Med.* **76**, 1574–1581 (2016).
- 948 65. Jerome, N. P. *et al.* Extended T2-IVIM model for correction of TE dependence of pseudo-diffusion
949 volume fraction in clinical diffusion-weighted magnetic resonance imaging. *Phys. Med. Biol.* **61**,
950 N667–N680 (2016).
- 951 66. Garyfallidis, E. *et al.* Dipy, a library for the analysis of diffusion MRI data. *Front. Neuroinform.* **8**, 8
952 (2014).
- 953 67. Ourselin, S., Roche, A., Subsol, G., Pennec, X. & Ayache, N. Reconstructing a 3D structure from
954 serial histological sections. *Image Vis. Comput.* **19**, 25–31 (2001).
- 955 68. Andersson, J. L. R., Skare, S. & Ashburner, J. How to correct susceptibility distortions in spin-echo
956 echo-planar images: application to diffusion tensor imaging. *Neuroimage* **20**, 870–888 (2003).
- 957 69. Avants, B. B., Epstein, C. L., Grossman, M. & Gee, J. C. Symmetric diffeomorphic image
958 registration with cross-correlation: evaluating automated labeling of elderly and neurodegenerative
959 brain. *Med. Image Anal.* **12**, 26–41 (2008).
- 960 70. Rafael-Patino, J. *et al.* Robust Monte-Carlo Simulations in Diffusion-MRI: Effect of the Substrate
961 Complexity and Parameter Choice on the Reproducibility of Results. *Front. Neuroinform.* **14**, 8
962 (2020).

963

964

965

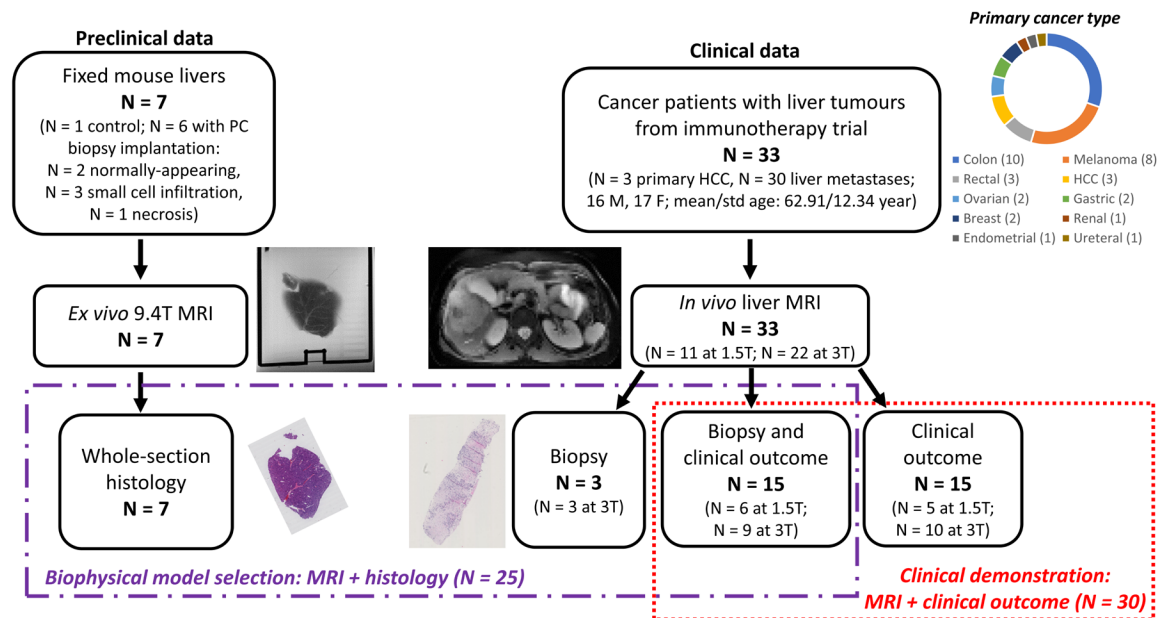
966

967

968

969

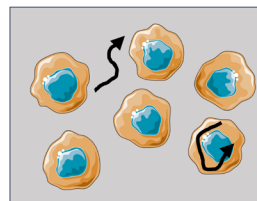
970 **Figures**



971

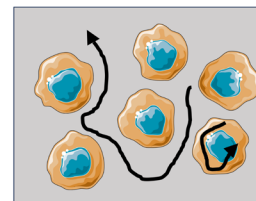
972 **Fig. 1. Illustration of the liver MRI and histology data used in the study.** Our data set consisted
 973 of preclinical and clinical data. The preclinical data encompasses dMRI scans of seven fixed livers
 974 from mice (six implanted with tissue from biopsies of patients suffering from prostate cancer; one
 975 without any implantation). We scanned the livers *ex vivo* on a 9.4T system, and obtained HE
 976 histological sections at known position. The clinical data includes *in vivo* liver dMRI scans
 977 performed on 33 patients suffering from advanced liver tumours. Scans were performed on clinical
 978 1.5T and 3T MRI systems. For 18 patients, HE-stained material from a biopsy taken from one of
 979 the imaged liver tumours was also available. 30 out of 33 patients effectively participated in a
 980 phase I immunotherapy trial, and clinical outcome was available as PFS. We used a total sample
 981 size of N = 25 for dMRI model design and of N = 30 for response assessment. In the figure, PC
 982 standard fort prostate cancer and HCC for hepatocellular carcinoma.

(A) dMRI signal models



Models with no assumption on which of intra-/extra-cellular ADC is higher

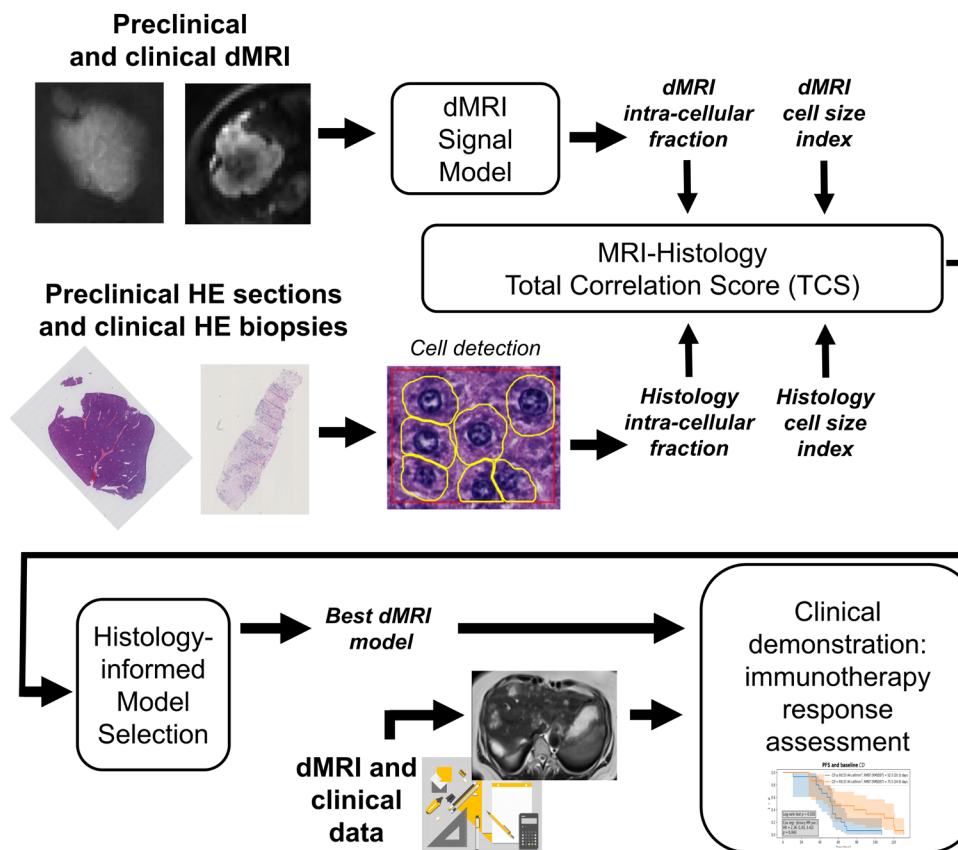
• *Diff-in-exTD* • *Diff-in-ex*



Models with higher extra-cellular ADC than intra-cellular ADC

• *Diff-in-exTDFast* • *Diff-in-exFast*
• *Diff-in*

(B) Study overview



983

984

985

986

987

988

989

990

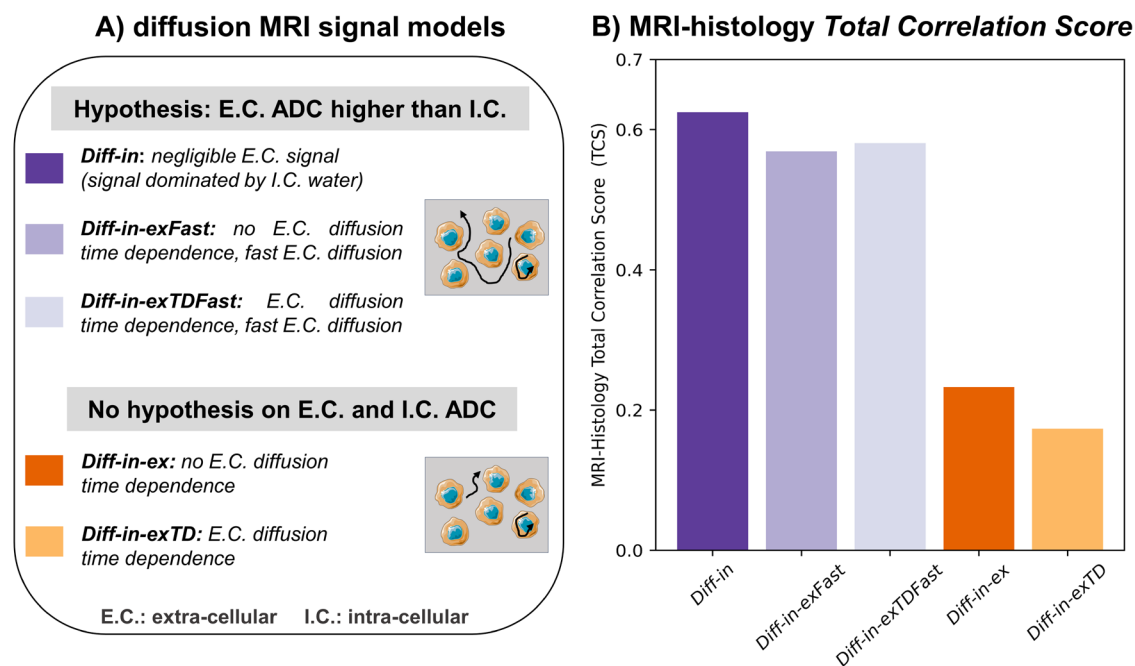
991

992

Fig. 2. Description of the dMRI signal models and study overview. (A), top: cartoon illustrating the two families of dMRI models considered in this study, consisting of 1) models with no assumption of which of intra-/extra-cellular ADC is higher, and 2) models where the extra-cellular ADC is hypothesised to be higher than the intra-cellular ADC. (B), bottom: study overview. We analysed dMRI data from fixed mouse livers (preclinical data) and from cancer patients imaged *in vivo* (clinical data) to derive estimates of intra-cellular fraction and of cell size. In parallel, we processed histological material from the same tissues (whole-liver sections for the preclinical mouse data; biopsies from one of the imaged tumours for the clinical data), and derived the histological counterparts of such dMRI metrics. We compared dMRI and histological cell size and

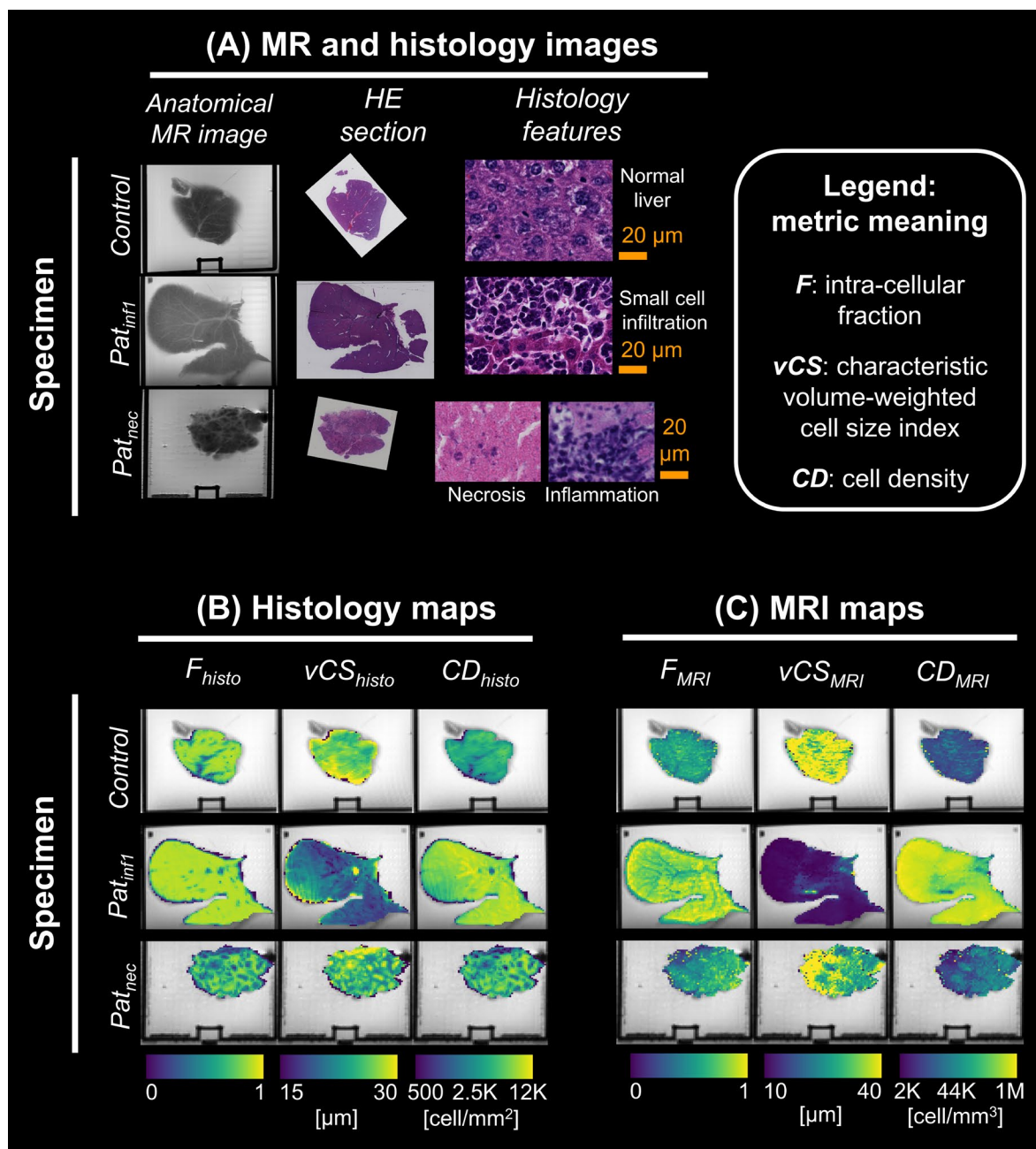
993 intra-cellular fraction to select the dMRI model featuring the best fidelity to histology. The utility
 994 of the model was then demonstrated in immunotherapy response assessment *in vivo*. In Fig. 2,
 995 pictures from Servier Medical Art have been used. Servier Medical Art by Servier is licensed under
 996 a Creative Commons Attribution 3.0 Unported License
 997 (<https://creativecommons.org/licenses/by/3.0/>).

998
 999
 1000
 1001



1002

1003 **Fig. 3. Biophysical dMRI signal model selection based on the MRI-histology Total**
 1004 **Correlation Score (TCS).** (A): panel summarising the salient differences between the biophysical
 1005 dMRI models compared in this study. Models can be divided in two families, i.e.: i) models where
 1006 it is hypothesised that the extra-cellular ADC is higher than the intra-cellular ADC, and ii) models
 1007 with no hypothesis on which, between intra-/extra-cellular ADC is higher. Violet shades are used
 1008 for the first family (models *Diff-in*, *Diff-in-exFast* and *Diff-in-exTDFast*), while orange shades for
 1009 the second family (models *Diff-in-ex* and *Diff-in-exTD*). (B): values of TCS for all models, as
 1010 obtained by fitting them on high b-value images ($b > 1800$ s/mm² in the fixed mouse livers; $b >$
 1011 900 s/mm² *in vivo*). We performed model selection using a sample size of $N = 25$ (see Fig. 1). In
 1012 Fig. 3, pictures from Servier Medical Art have been used. Servier Medical Art by Servier is
 1013 licensed under a Creative Commons Attribution 3.0 Unported License
 1014 (<https://creativecommons.org/licenses/by/3.0/>).



1015

1016

1017

1018

1019

1020

1021

1022

1023

1024

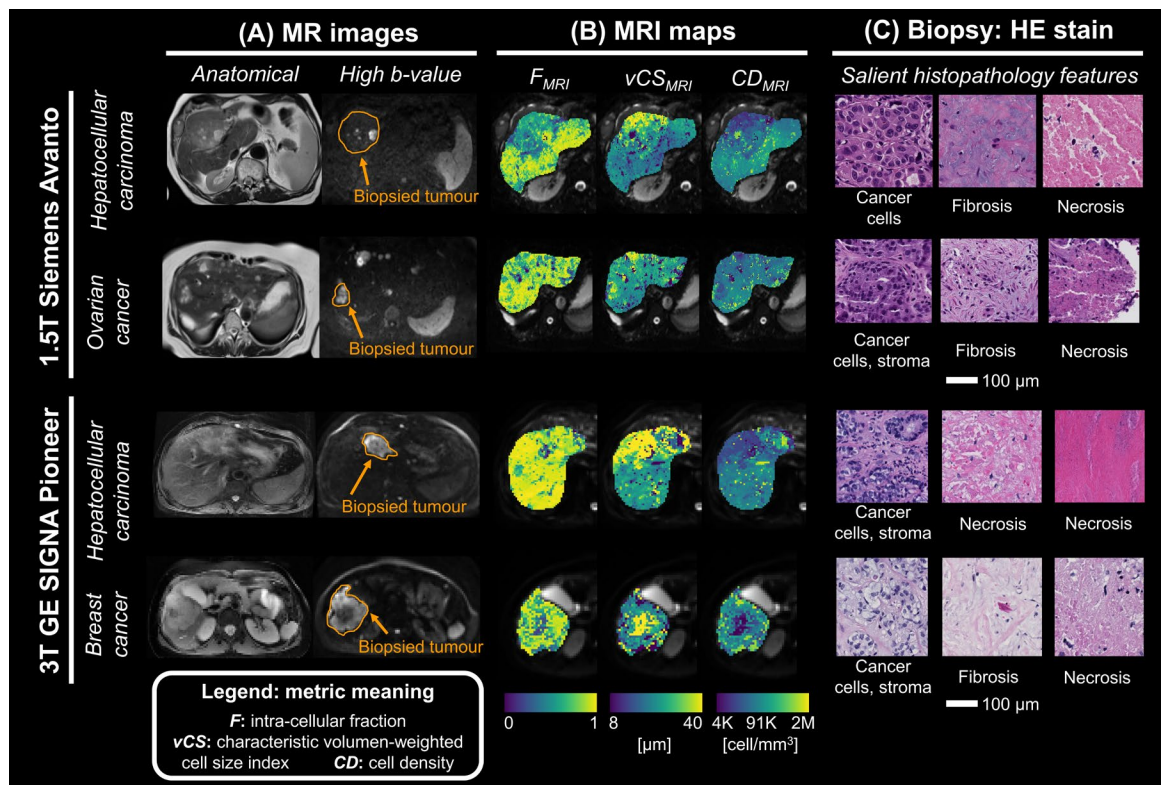
Fig. 4. Maps from the selected dMRI model *Diff-in* with their histological counterparts in the fixed mouse livers scanned at 9.4T *ex vivo*. The figure reports MRI and histology data for 3 specimens, representative of the 3 microstructural phenotypes observed in our *ex vivo* data set, namely: normal liver structures (*Control* case); a proliferative process, characterized by infiltration of small cells (*Pat_{infl}* case); necrosis and inflammation (*Pat_{nec}* case). For all specimens, the following is shown. **(A)**, *top left*: a high-resolution T2-w anatomical scan is shown next to the corresponding HE section, with histological details. **(B)**, *bottom left*: histological maps warped to the dMRI space (intra-cellular patch area fraction F_{histo} ; volume-weighted mean cell size index vCS_{histo} ; cell density per unit patch area CD_{histo}). **(D)**, *bottom right*: dMRI maps F_{MRI} , vCS_{MRI}

1025 and CD_{MRI} from the selected dMRI signal model (model *Diff-in*, fitted to high b -value images, i.e.,
 1026 $b > 1800 \text{ s/mm}^2$).

1027

1028

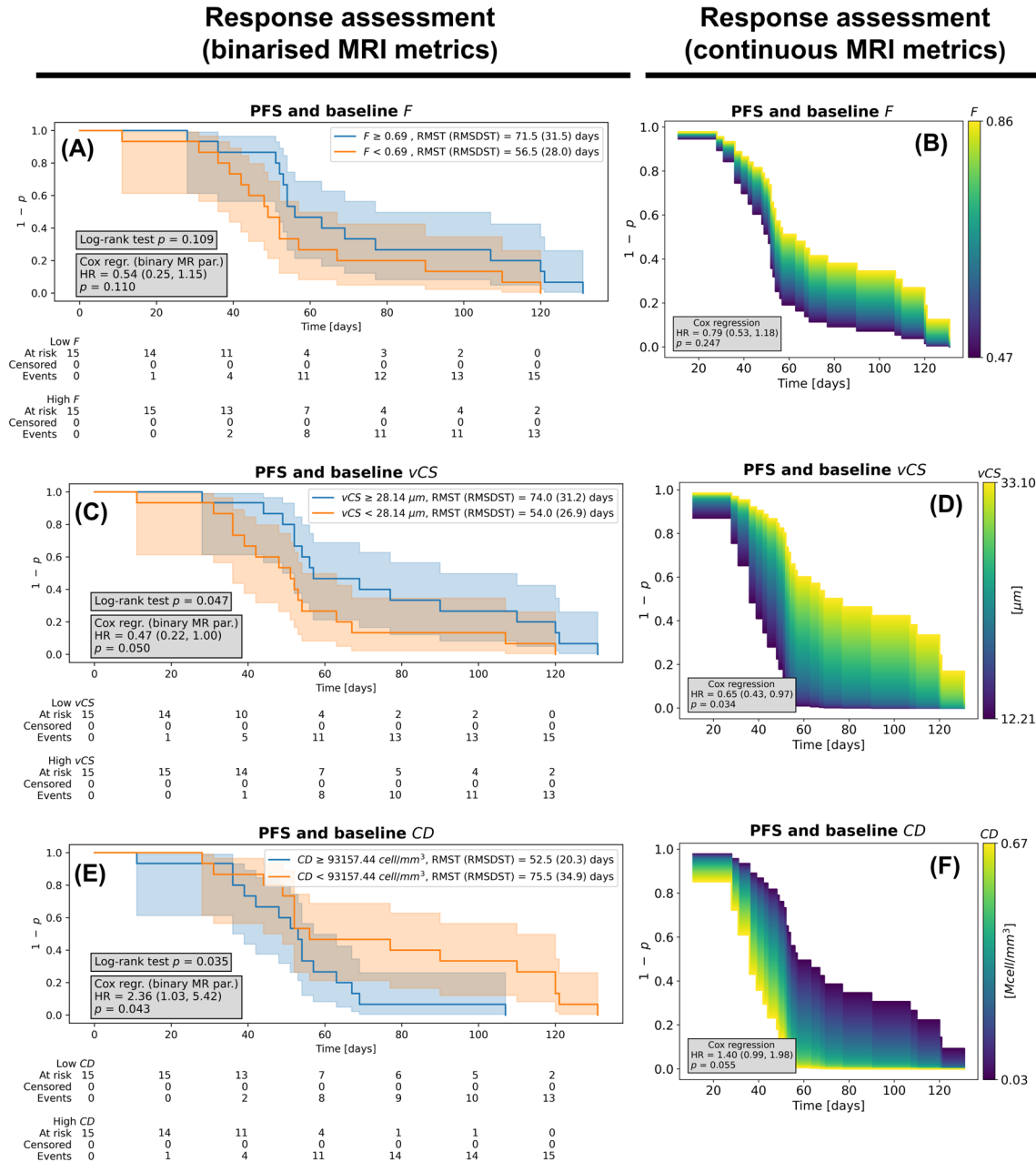
1029



1030

1031 **Fig. 5. Examples of maps from the proposed dMRI model *Diff-in* in liver tumours of patients**
 1032 **scanned at 1.5T and 3T *in vivo*, with co-localised biopsies. MRI maps are shown in a biopsied**
 1033 **liver tumour in two patients for each MRI scanner, arranged along rows. (A): examples of slices**
 1034 **from the high-resolution anatomical T2-w image and from a high b-value image, with biopsied**
 1035 **tumour outlined. (C): maps from the selected model (*Diff-in*, fitted to high b-value images $b > 900$**
 1036 **s/mm^2). From left to right: intra-cellular signal fraction F_{MRI} ; volume-weighted mean cell size**
 1037 **index vCS_{MRI} ; cell density per unit volume CD_{MRI} . (C): histological details from the HE-stained**
 1038 **biopsy. For the 1.5T Siemens scanner (first and second rows from top) we report: patient 6**
 1039 **(primary hepatocellular carcinoma) and patient 3 (liver metastases from ovarian cancer). For the**
 1040 **3T GE scanner (third and fourth rows from top) we report: patient 24 (primary hepatocellular**
 1041 **carcinoma (HCC)) and patient 30 (liver metastases from breast cancer).**

1042



1043

1044

1045

1046

1047

1048

1049

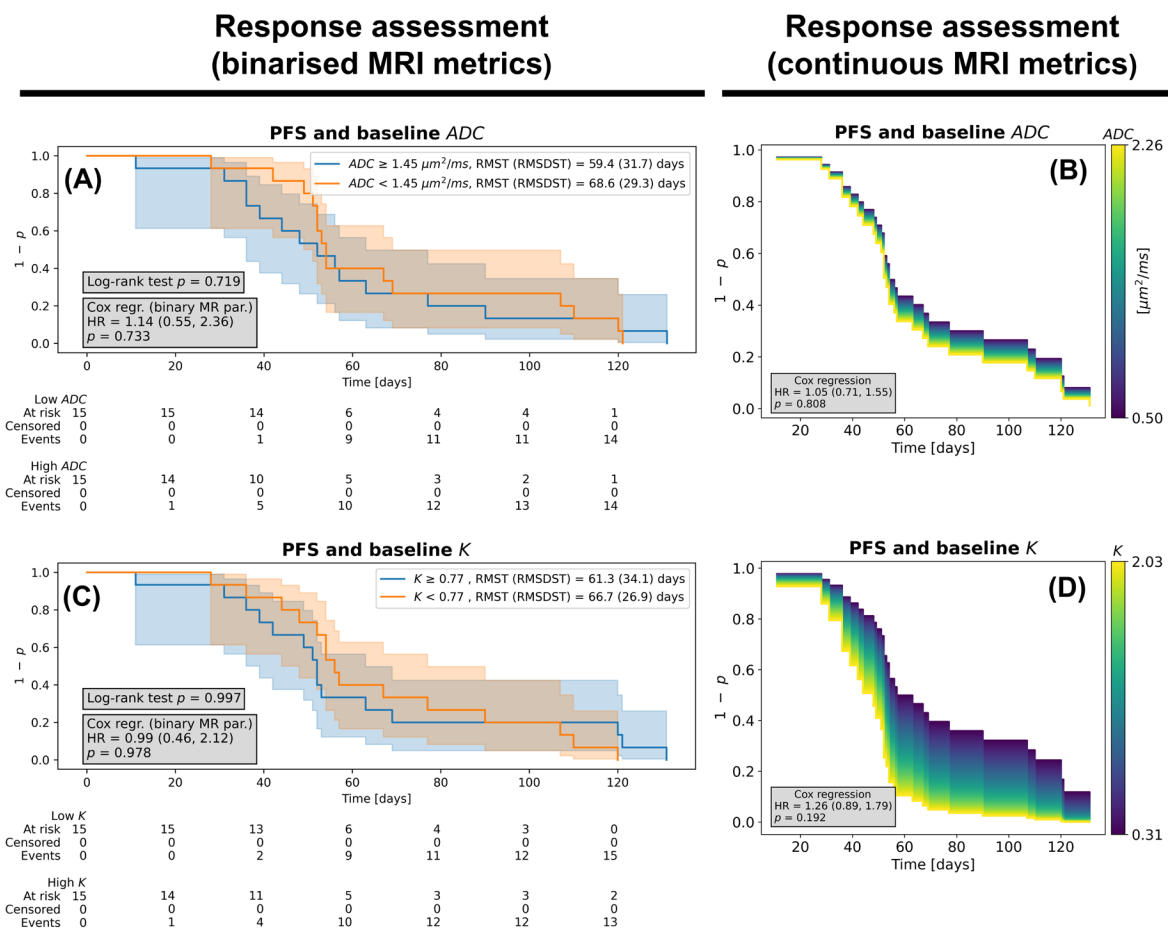
1050

1051

Fig. 6. Immunotherapy response assessment based on metrics from the proposed model *Diff-in* within liver tumours at baseline. This figure reports on the dependence of patients' progression-free survival (PFS) on the average value of F , vCS and CD within liver tumours at baseline (i.e., before starting immunotherapy), as obtained by fitting model *Diff-in* at high b-value. *Left*: Kaplan-Meier (KM) survival curves of two groups obtained by splitting patients based on baseline F (panel A), vCS (panel C) and CD (panel D) (lower/higher than the sample median). The grey panel reports the p-values of a log-rank sum test comparing the KM curves, and of a Cox regression based on the binarised MRI metric (with the corresponding hazard ratio (HR) estimate

1052
1053
1054
1055
1056
1057
1058
1059
1060
1061

and 95% confidence interval). The legend reports the Restricted Mean Survival Time (RMST) and Restricted Standard Deviation of Survival Time (RSDST) for each KM curve. *Right*: results from univariate Cox regression where the baseline F (panel B), vCS (panel D) and CD (panel F) is a continuous predictor of the survival. The panel shows how changes in baseline F , vCS and CD modulate the survival curve, given the HR estimated for each metric. In the grey box, the p-value and HR (with 95% CI) corresponding to the baseline MRI metric are reported. In all panels, the y-axis shows $1 - p$, with p being the probability of progression, while the x-axis shows the time to progression (in days). We performed the response assessment using a sample size of $N = 30$ (Fig. 1).



1062
1063
1064
1065
1066
1067

Fig. 7. Immunotherapy response assessment based on mean ADC and kurtosis K within liver tumours at baseline. This figure reports on the dependence of patients' progression-free survival (PFS) on the average value of ADC and K within liver tumours at baseline (i.e., before starting immunotherapy). *Left*: Kaplan-Meier (KM) survival curves of two groups obtained by splitting patients based on baseline ADC (panel A) and K (panel C) (lower/higher than the sample median).

1068 The grey panel reports the p-values of a log-rank sum test comparing the KM curves, and of a Cox
 1069 regression based on the binarised MRI metric (with the corresponding hazard ratio (HR) estimate
 1070 and 95% confidence interval). The legend reports the Restricted Mean Survival Time (RMST) and
 1071 Restricted Standard Deviation of Survival Time (RSDST) for each KM curve. *Right*: results from
 1072 univariate Cox regression where the baseline *ADC* (panel B) and *K* (panel D) is a continuous
 1073 predictor of the survival. The panel shows how changes in baseline *ADC* and *K* modulate the
 1074 survival curve, given the HR estimated for each metric. In the grey box, the p-value and HR (with
 1075 95% CI) corresponding to the baseline MRI metric are reported. In all panels, the y-axis shows 1
 1076 $- p$, with p being the probability of progression, while the x-axis shows the time to progression (in
 1077 days). We performed the response assessment using a sample size of $N = 30$ (Fig. 1).

1078

1079 **Tables**

1080 **Table 1. Correlation between dMRI metrics and histological metrics.** The table reports
 1081 Pearson’s correlation coefficients r and corresponding p-values p of dMRI metrics F_{MRI} (intra-
 1082 cellular fraction), vCS_{MRI} (volume-weighted cell size index) and CD_{MRI} (cell density per unit
 1083 volume) with their histological pairs (F_{histo} , vCS_{histo} and CD_{histo} respectively) for the selected
 1084 dMRI model (*Diff-in*, fitted to high b-value images). The table also reports correlation coefficients
 1085 between routine ADC and *K* from DKI and each of F_{histo} , vCS_{histo} and CD_{histo} . The sample size
 1086 was $N = 25$, so that $p < 0.05$ if $|r| > 0.3961$. When $p < 0.05$, grey shadowing is used.

dMRI technique	Histology F_{histo}	Histology vCS_{histo}	Histology CD_{histo}
Model	With F_{MRI} :	With vCS_{MRI} :	With CD_{MRI} :
<i>Diff-in</i>	$r = 0.19; p = 0.37$	$r = 0.44; p = 0.029$	$r = 0.70; p = 0.0001$
Routine	With ADC: $r = -0.28; p = 0.18$	With ADC: $r = 0.49; p = 0.014$	With ADC: $r = -0.47; p = 0.017$
DKI	With <i>K</i> : $r = 0.40; p = 0.048$	With <i>K</i> : $r = -0.31; p = 0.13$	With <i>K</i> : $r = 0.43; p = 0.033$

1087

Supplementary Information for

Histology-informed liver diffusion MRI: biophysical model design and demonstration in cancer immunotherapy

Francesco Grussu*, Kinga Bernatowicz, Marco Palombo, Irene Casanova-Salas, Ignasi Barba, Sara Simonetti, Garazi Serna, Athanasios Grigoriou, Anna Voronova, Valezka Garay, Juan Francisco Corral, Marta Vidorreta, Pablo García-Polo García, Xavier Merino, Richard Mast, Núria Roson, Manuel Escobar, Maria Vieito, Rodrigo Toledo, Paolo Nuciforo, Joaquin Mateo, Elena Garralda, Raquel Perez-Lopez*

*Corresponding authors: Francesco Grussu, email: fgrussu@vhio.net, Raquel Perez-Lopez, email: rperez@vhio.net

Table of contents

- Supplementary Fig. S1:** radiological-histological co-localisation of the *ex vivo* mouse liver data.
 - Supplementary Fig. S2:** MRI-histology Total Correlation Score (TCS) for biophysical dMRI model selection, as obtained when fitting dMRI signal models on the whole image set.
 - Supplementary Fig. S3:** biophysical dMRI signal model selection based on BIC and HFC criteria.
 - Supplementary Fig. S4:** biophysical model selection across different MRI scanners and data subsets.
 - Supplementary Fig. S5:** environments used to generate synthetic dMRI signals in computer simulations.
 - Supplementary Fig. S6:** MRI-histology correlations for models with no assumptions on which is larger between intra-cellular and extra-cellular ADC.
 - Supplementary Fig. S7:** MRI-histology correlations for models where the extra-cellular ADC is constrained to be larger than the intra-cellular ADC.
 - Supplementary Fig. S8:** standard diffusion MRI metrics in fixed mouse livers *ex vivo*.
 - Supplementary Fig. S9:** key parametric maps of the *Diff-in-exFast* model on *ex vivo* mouse livers.
 - Supplementary Fig. S10:** diffusivity metrics from biophysical MRI models in fixed *ex vivo* mouse livers.
 - Supplementary Fig. S11:** standard diffusion MRI metrics in patients *in vivo*.
 - Supplementary Fig. S12:** key parametric maps of the *Diff-in-exFast* model in patients *in vivo*.
 - Supplementary Fig. S13:** diffusivity metrics from biophysical MRI models in patients *in vivo*.
 - Supplementary Fig. S14:** immunotherapy response assessment based on *Diff-in* cytosol diffusivity estimates.
 - Supplementary Fig. S15:** immunotherapy response assessment based on vascular fraction estimates.
 - Supplementary Fig. S16:** immunotherapy response assessment based on *Diff-in-exFast* MRI metrics.
 - Supplementary Fig. S17:** schematic of the dMRI sequences used in this study.
- Supplementary Table S1:** results of the model selection based on the Total Correlation Score (TCS) as obtained on simulated dMRI signals.

Supplementary Table S2: results of the model selection based on the Histology Fidelity Criterion (HFC) as obtained on simulated dMRI signals.

Supplementary Table S3: results of the model selection based on the Bayesian Information Criterion (BIC) as obtained on simulated dMRI signals.

Supplementary Table S4: descriptive statistics of histology and MRI metrics in the fixed mouse livers.

Supplementary Table S5: hazard ratios obtained from Cox regression models controlling for sex, age, and baseline tumour volume.

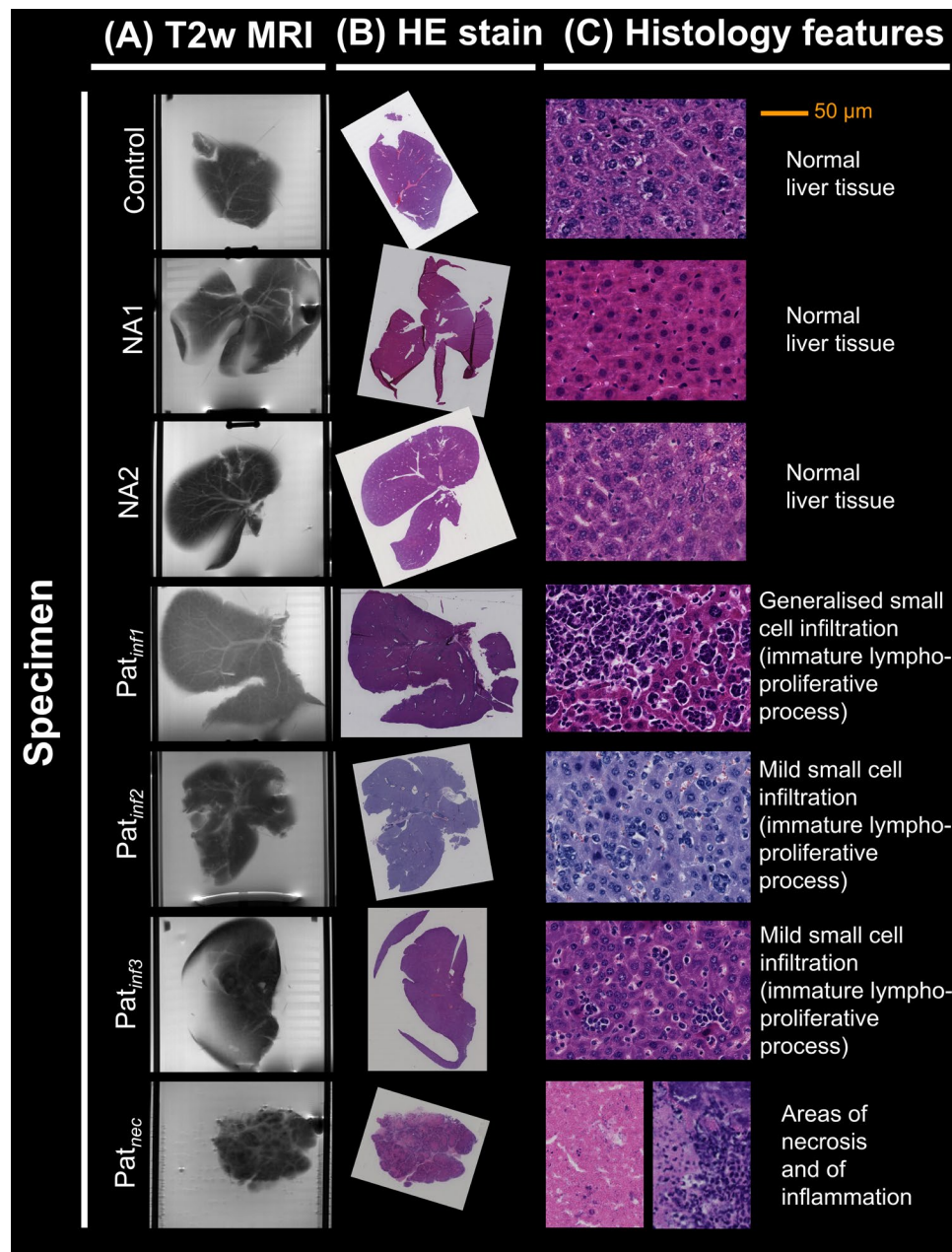


Fig. S1: radiological-histological co-localisation of the *ex vivo* mouse liver data.

Illustration of the radiological-histological co-localisation on the 7 fixed mouse livers obtained from mice implanted with a biopsy from a prostate cancer patient. (A), left: illustrative slice of the high-resolution anatomical T2-weighted fast spin echo. (B), centre: hematoxylin and eosin (HE)-stained section, taken from the MRI slice shown to the left. (C), right: detail of the microstructure characterising each specimen, as assessed by an experienced pathologist (SS). Different specimens are arranged along different rows. From top to bottom: *Control*, normal liver structures (no biopsy implantation); *Pat_{NA1}* and *Pat_{NA2}*, normal appearing normal liver structures after prostate cancer biopsy implantation; *Pat_{inf1}*, *Pat_{inf2}* and *Pat_{inf3}*: pathology following implantation, consisting of an immature, lympho-proliferative process (infiltration of small cells in sinusoidal spaces); *Pat_{nec}*, pathology following implantation, consisting of necrosis and inflammation.

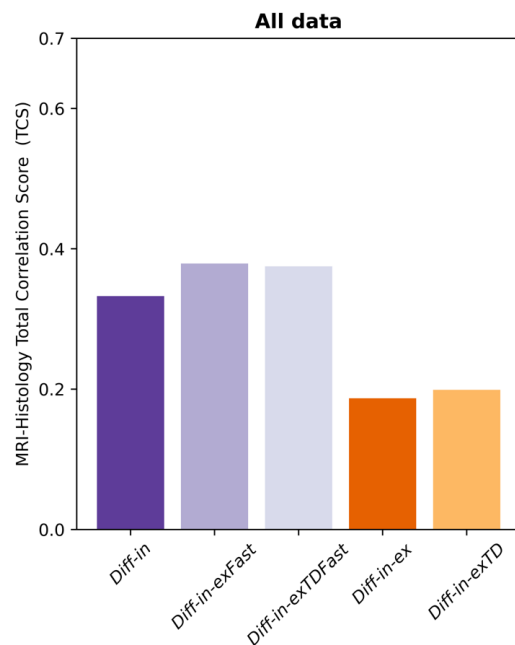


Fig. S2: MRI-histology Total Correlation Score (TCS) for biophysical dMRI model selection, as obtained when fitting dMRI signal models on the whole image set.

Values of TCS for all models, as obtained by fitting models on the whole image set (set of images with negligible vascular signal contributions, i.e., $b > 1000$ s/mm² in the fixed mouse livers and $b > 100$ s/mm² *in vivo*). We evaluated TCS for histology-informed model selection using a sample size of $N = 25$.

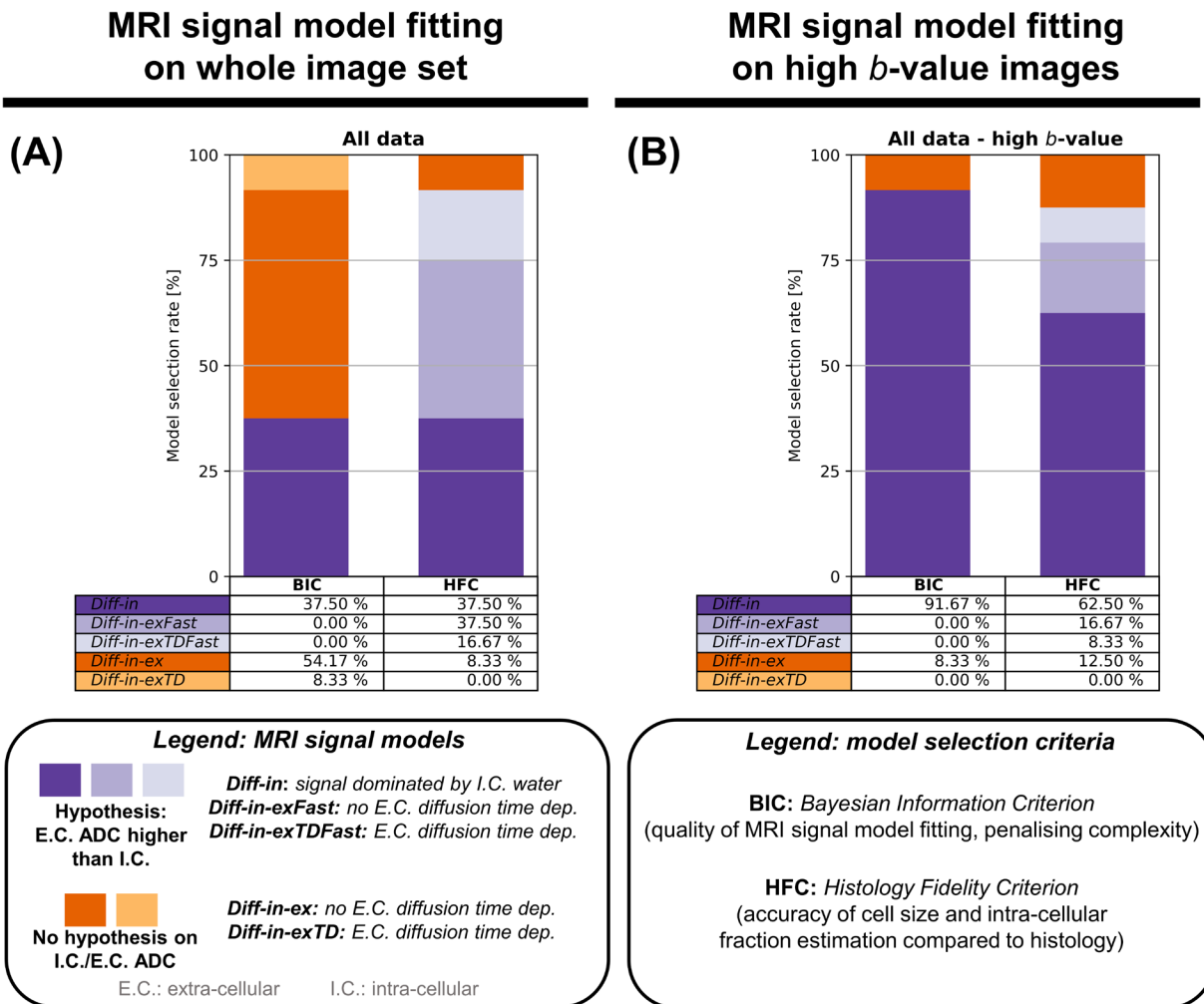


Fig. S3: biophysical dMRI signal model selection based on BIC and HFC criteria.

Frequency of model selection based on the *Bayesian Information Criterion* (BIC, quantifying how well a model fits the dMRI signals, penalising model complexity) and on the *Histology-fidelity Criterion* (HFC, quantifying how accurately a dMRI models estimates the intra-cellular fraction and the volume-weighted cell size as seen on histology). (A) reports results when models are fitted to the entire set of measurements with negligible vascular signal contributions ($b > 1000$ s/mm² for suppression of PBS fluid within vessels in the fixed mouse livers; $b > 100$ s/mm² for IVIM signal suppression *in vivo* on clinical systems), while (B) reporting results obtained when fitting models only on high b -value images ($b > 1800$ s/mm² in the fixed mouse livers; $b > 900$ s/mm² *in vivo*).

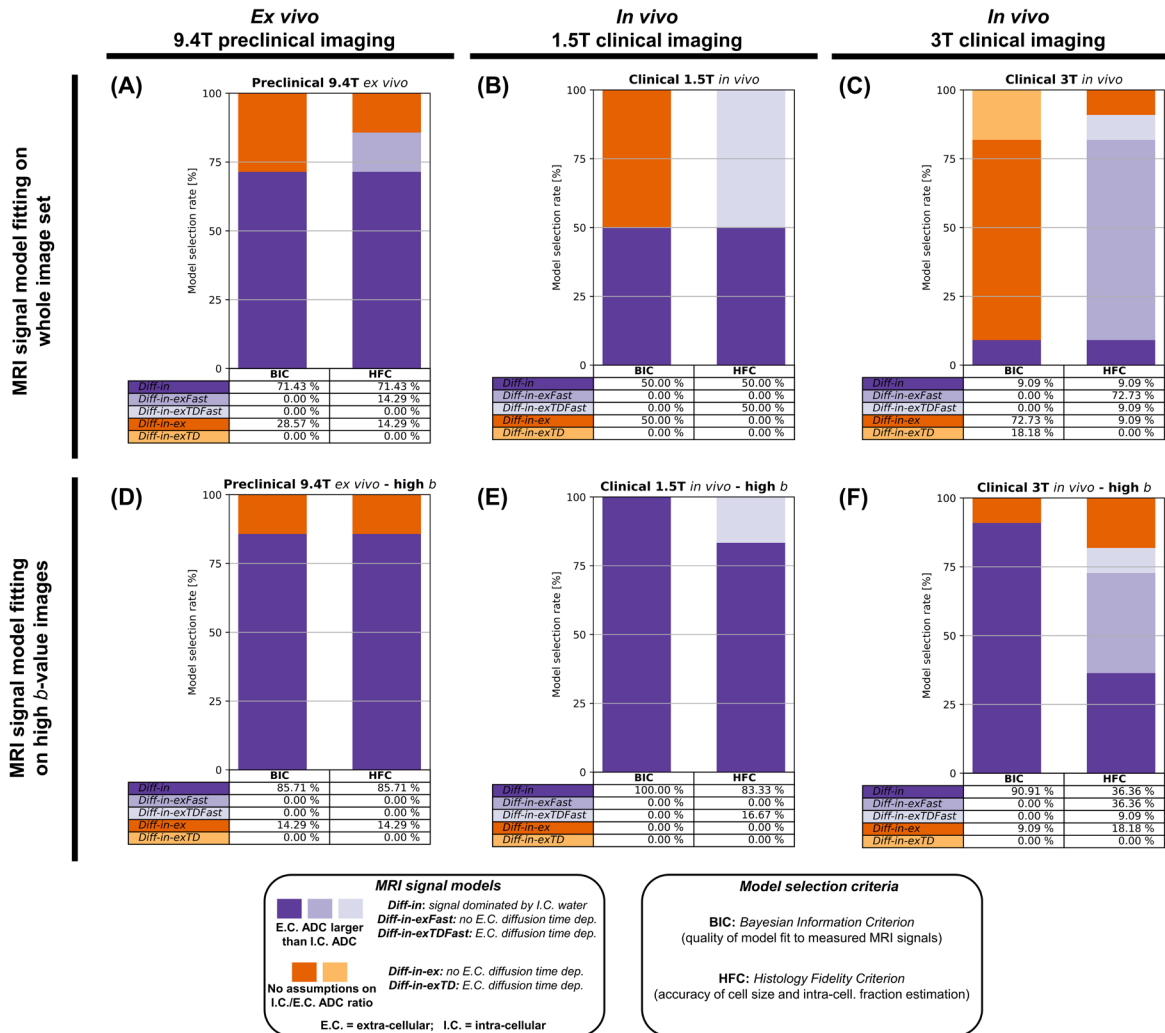


Fig. S4: biophysical model selection across different MRI scanners and data subsets.

Frequency of selection of each of 5 biophysical dMRI models on 3 MRI-histology data subsets. First column: selection on 7 fixed mouse livers scanned *ex vivo* on a preclinical 9.4T Bruker system (A and D, left); Second column: selection on 6 liver tumours imaged *in vivo* on a clinical 1.5T Siemens system (B and E, middle); Third column: selection on 12 liver tumours imaged *in vivo* on a clinical 3T GE system (C and F, right). Plots on top (A to C) refer to dMRI model fitting performed on images where the vascular signal was suppressed (“whole image set fitting”, $b > 1000$ s/mm² for suppression of PBS fluid within vessels on the 9.4T; $b > 100$ s/mm² for IVIM signal suppression on clinical systems). Plots to the bottom (D to F) refer to dMRI model fitting performed on images where both vascular and extra-cellular, extra-vascular signals were suppressed (“high b-value fitting”, $b > 1800$ s/mm² on the 9.4T; $b > 900$ s/mm² on clinical systems). Violet: models where extra-cellular ADC is larger than intra-cellular ADC; orange: models with no constraints on which is larger between intra-/extra-cellular ADC. The *Bayesian Information Criterion* (BIC) selects a model depending on the goodness of MRI signal fitting. The *Histology Fidelity Criterion* (HFC) selects a model depending on the overall agreement between MRI volume-weighted Cell Size (vCS) and intra-cellular fraction (F) with their histology counterparts.

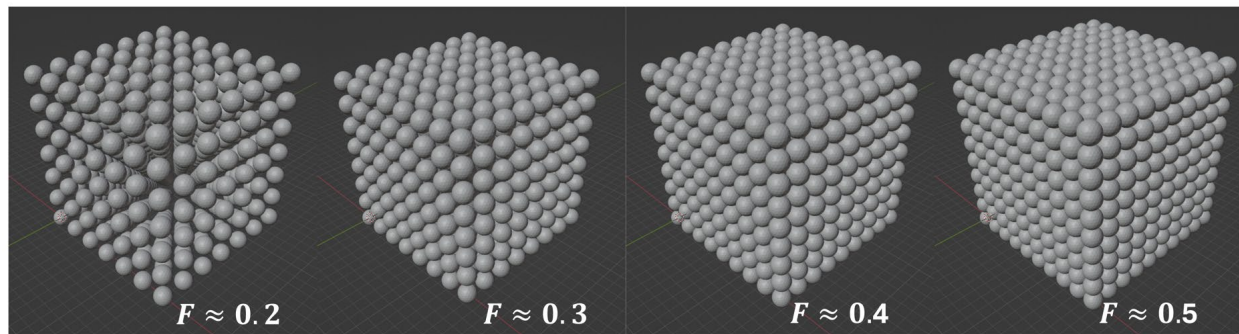


Fig. S5: environments used to generate synthetic dMRI signals in computer simulations.

The synthetic environment consisted of meshed spheres of fixed diameter, representing cells, as this is a common biophysical model used in several dMRI techniques (e.g., VERDICT, IMPULSED). We used the synthetic environment to generate dMRI signals via Monte Carlo simulations for each of the 3 dMRI protocols considered in this study (the PGSE protocol used on the *ex vivo* mouse livers at 9.4T; the PGSE protocol used in patients *in vivo* at 3T; the DW TRSE protocol used in patients *in vivo* at 1.5T). Afterwards, we performed dMRI model selection on the synthetic signals, following the same procedures implemented for actual *ex vivo* and *in vivo* dMRI data. We controlled the intra-sphere fraction F by adding gaps of increasing size in-between abutting spheres packed in an ideal cubic lattice. We probed 4 different values of F (approximately equal to 0.197, 0.323, 0.406, 0.523; notice that the maximum theoretical value of F for cubic lattice packing is equal to 0.5236). For each value of F , we varied the cell diameter (8, 16, 22 and 30 μm), intra-sphere diffusivity (10 linearly-spaced values in the ranges $[0.8; 2.6] \mu\text{m}^2 \text{ms}^{-1}$ and $[0.8; 3.0] \mu\text{m}^2 \text{ms}^{-1}$ for the *ex vivo* and *in vivo* protocols respectively) and extra-sphere intrinsic diffusivity (again, 10 linearly-spaced values in the ranges $[0.8; 2.6] \mu\text{m}^2 \text{ms}^{-1}$ and $[0.8; 3.0] \mu\text{m}^2 \text{ms}^{-1}$ for the *ex vivo* and *in vivo* protocols respectively), generating a total of 1600 synthetic voxels. Before dMRI signal model fitting, we corrupted synthetic signal with Rician noise at a signal-to-noise ratio (SNR) of 30 on the $b = 0$ signal $s(b=0)$ ($\text{SNR} = s(b=0)/\sigma$, where σ is the noise standard deviation).

Model fitting on whole image set Model fitting on high b -value images

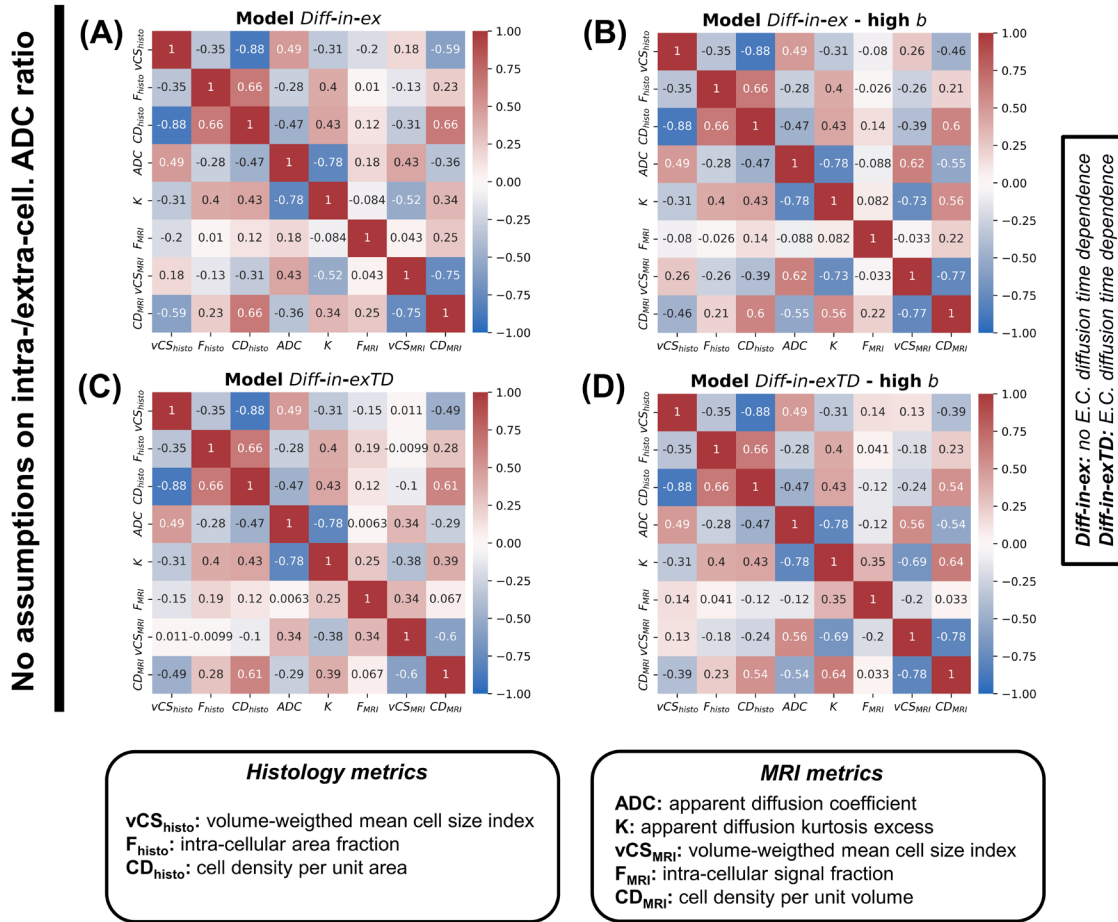


Fig. S6: MRI-histology correlations for models with no assumptions on which is larger between intra-cellular and extra-cellular ADC. Matrices illustrating Pearson's correlation coefficients among all possible pairs of MRI and histology metrics. Histological metrics are: intra-cellular area fraction F_{histo} ; volume-weighted mean cell size index vCS_{histo} ; cell density per unit area CD_{histo} . MRI metrics are: apparent diffusion coefficient ADC ; apparent diffusion excess kurtosis K ; intra-cellular area fraction F_{MRI} ; volume-weighted mean cell size index vCS_{MRI} ; cell density per unit area CD_{MRI} . Metrics F_{MRI} , vCS_{MRI} and CD_{MRI} were obtained by fitting models with no assumptions on which is larger between intra-cellular and extra-cellular ADC (*Diff-in-ex* and *Diff-in-exTD*). The 4 panels refer to models *Diff-in-ex* and *Diff-in-exTD* fitted according to 2 different strategies. Panel (A): model *Diff-in-ex* fitted on the whole set of measurements with vascular signal suppression ($b > 100$ s/mm² *in vivo*, $b > 1000$ s/mm² *ex vivo*); panel (B): model *Diff-in-ex* fitted on high b -value measurements ($b > 900$ s/mm² *in vivo*, $b > 1800$ s/mm² *ex vivo*); panel (C): model *Diff-in-exTD* fitted on the whole set of measurements with vascular signal suppression; panel (D): model *Diff-in-exTD* fitted on high b -value measurements. We calculated correlation coefficients using a sample size of $N = 25$ (Fig. 1).

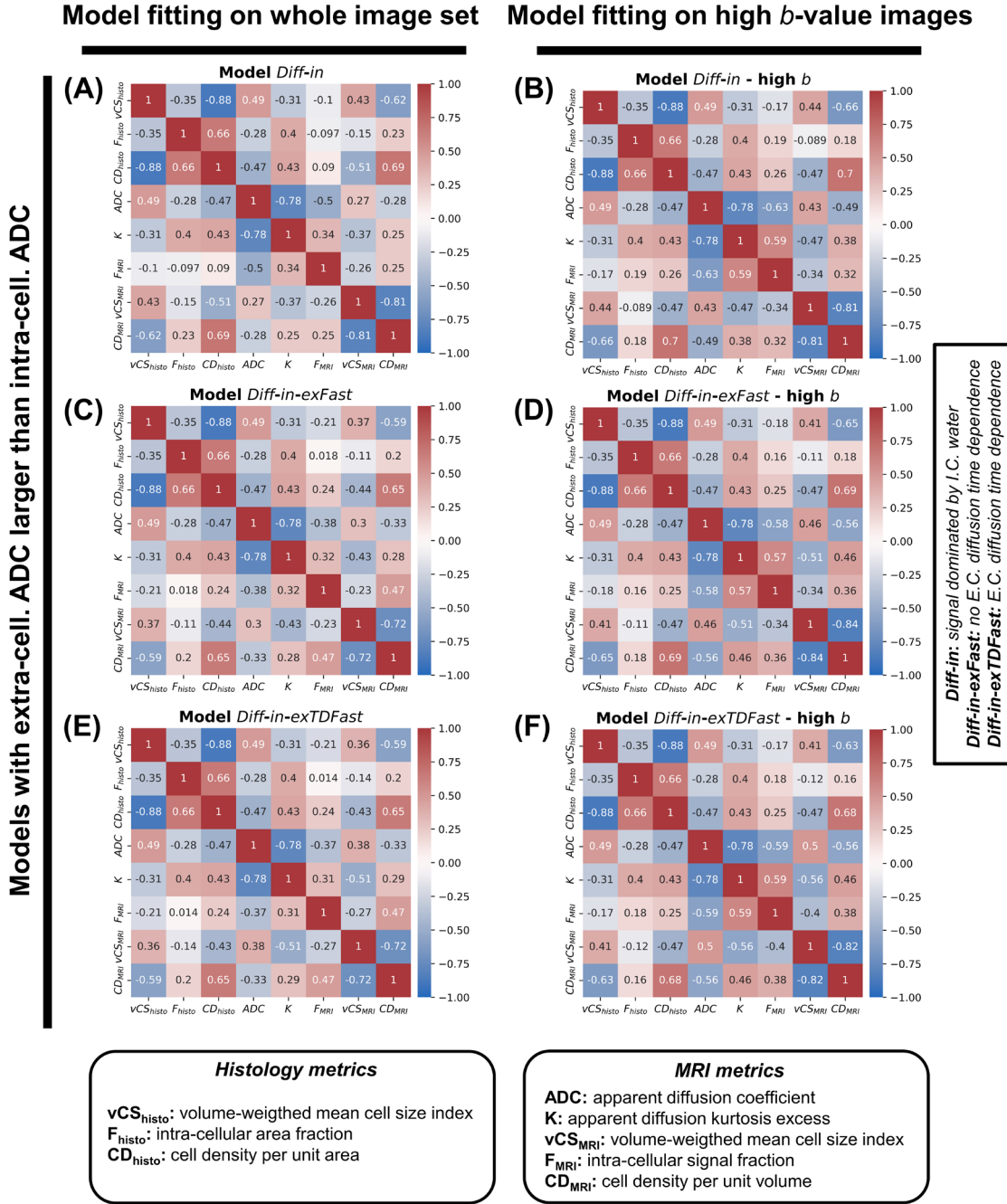


Fig. S7: MRI-histology correlations for models where the extra-cellular ADC is constrained to be larger than the intra-cellular ADC. Matrices illustrating Pearson's correlation coefficients among all possible pairs of MRI and histology metrics. Histological metrics are: intra-cellular area fraction F_{histo} ; volume-weighted mean cell size index vCS_{histo} ; cell density per unit area CD_{histo} . MRI metrics are: apparent diffusion coefficient ADC ; apparent diffusion excess kurtosis K ; intra-cellular area fraction F_{MRI} ; volume-weighted mean cell size index vCS_{MRI} ; cell density per unit area CD_{MRI} . Metrics F_{MRI} , vCS_{MRI} and CD_{MRI} were obtained by fitting models that assume that the extra-cellular ADC is always larger than the intra-cellular ADC (*Diff-in*, *Diff-in-exFast* and *Diff-in-exTDFast*). The 6 panels refer to models *Diff-in*, *Diff-in-exFast* and *Diff-in-exTDFast* fitted

according to 2 different strategies. Panel (A): model *Diff-in* fitted on the whole set of measurements with vascular signal suppression ($b > 100 \text{ s/mm}^2$ *in vivo*, $b > 1000 \text{ s/mm}^2$ *ex vivo*); panel (B): model *Diff-in* fitted on high b-value measurements ($b > 900 \text{ s/mm}^2$ *in vivo*, $b > 1800 \text{ s/mm}^2$ *ex vivo*); panel (C): model *Diff-in-exFast* fitted on the whole set of measurements with vascular signal suppression; panel (D): model *Diff-in-exFast* fitted on high b-value measurements; panel (E): model *Diff-in-exTDFast* fitted on the whole set of measurements with vascular signal suppression; panel (F): model *Diff-in-exTDFast* fitted on high b-value measurements. We calculated correlation coefficients using a sample size of $N = 25$ (Fig. 1).

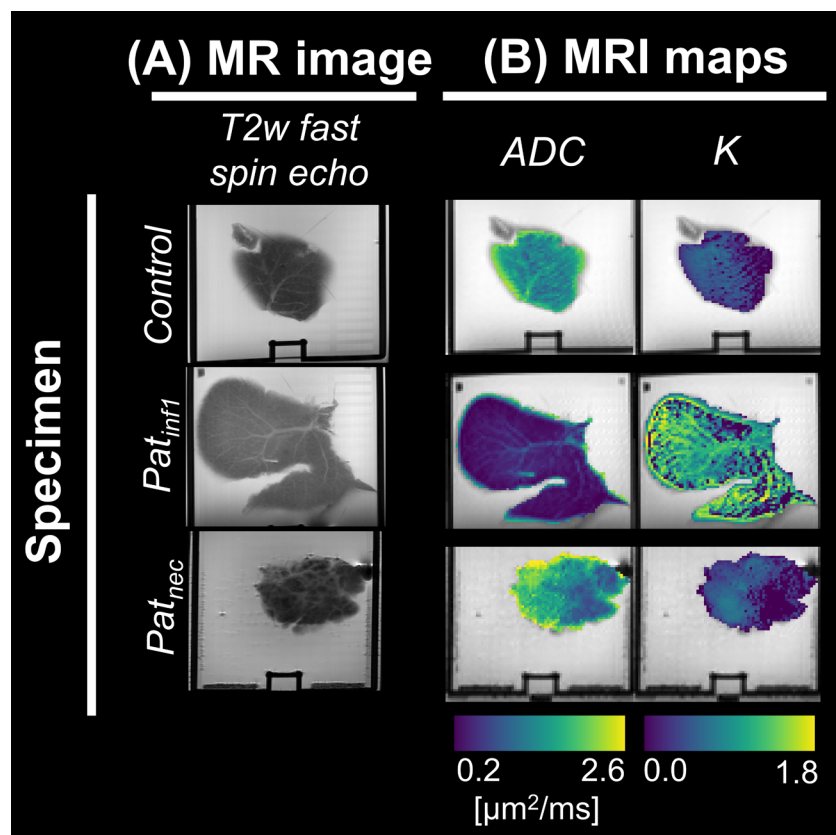


Fig. S8: standard diffusion MRI metrics in fixed mouse livers *ex vivo*.

(A): high-resolution fast spin echo scan acquired in fixed mouse livers scanned *ex vivo* on the 9.4T Bruker system. (B): standard diffusion metrics, namely *ADC* (apparent diffusion coefficient) and *K* (apparent diffusion kurtosis excess). These metrics were obtained by fitting the standard diffusion kurtosis signal representation $s = s_0 \exp(-b \text{ADC} + K (b \text{ADC})^2/6)$ to the set of measurements at fixed TE = 45 ms and $\Delta = 30$ ms. From top to bottom, the figure reports maps from 3 specimens, representative of the 3 different microstructural phenotypes seen in our mouse liver data. These are: normal liver structures (illustrated by the *Control* case, e.g., mouse with no biopsy implantation); pathology following biopsy implantation, consisting of an immature, lympho-proliferative process (infiltration of small cells in sinusoidal spaces, illustrated by case *Pat_{inf1}*); pathology following biopsy implantation, consisting of necrosis and inflammation (illustrated by case *Pat_{nec}*).

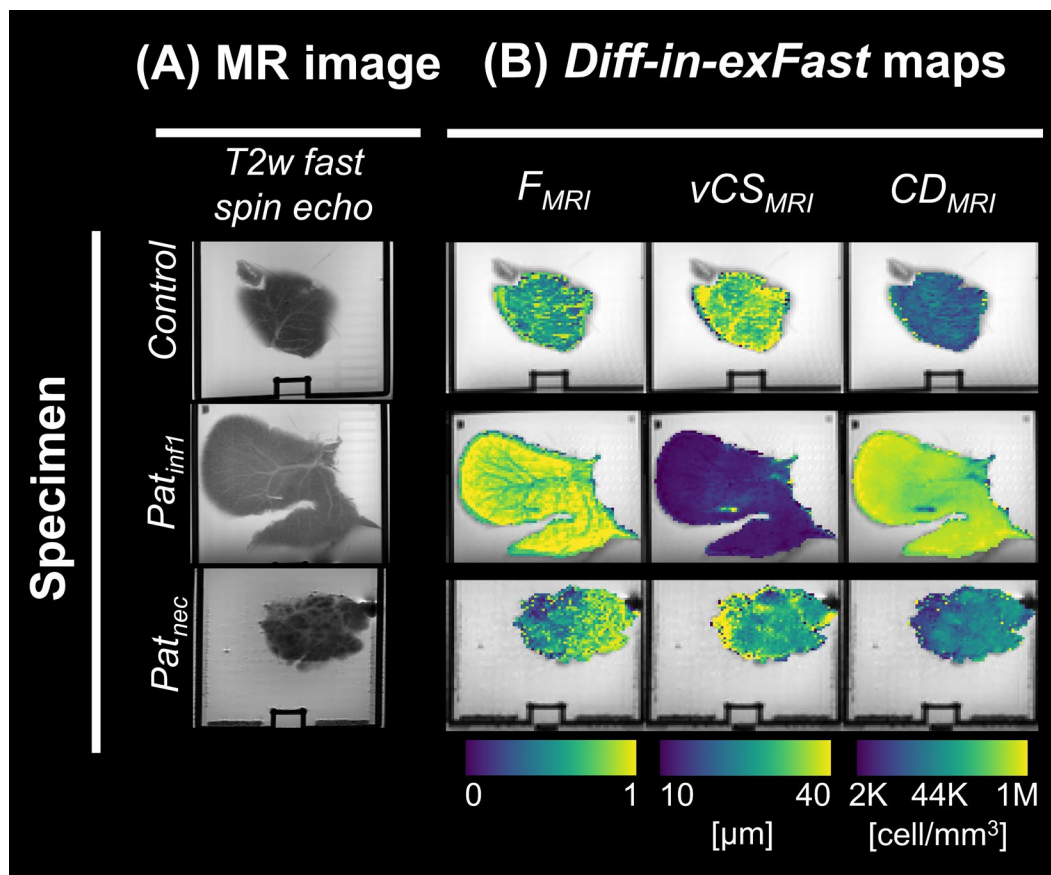


Fig. S9: key parametric maps of the *Diff-in-exFast* model on *ex vivo* mouse livers.

(A): high-resolution fast spin echo scan acquired in fixed mouse livers scanned *ex vivo* on the 9.4T Bruker system. (B): metrics from the *Diff-in-exFast* model fitted to the whole DW image set (b-values with negligible vascular signal contributions, i.e., $b > 1000$ s/mm² on fixed *ex vivo* tissue, to suppress signal from PBS-filled vessels). From left to right: intra-cellular signal fraction F_{MRI} ; volume-weighted cell size index vCS_{MRI} index; cell density per unit volume CD_{MRI} . Maps from 3 specimens are reported along different rows. The specimens are representative of the 3 different microstructural phenotypes seen in our mouse liver data. From top to bottom, these are: normal liver structures (illustrated by the *Control* case, e.g., mouse with no biopsy implantation); pathology following biopsy implantation, consisting of an immature, lympho-proliferative process (infiltration of small cells in sinusoidal spaces, illustrated by case *Pat_{inf1}*); pathology following biopsy implantation, consisting of extended necrosis and inflammation (illustrated by case *Pat_{nec}*).

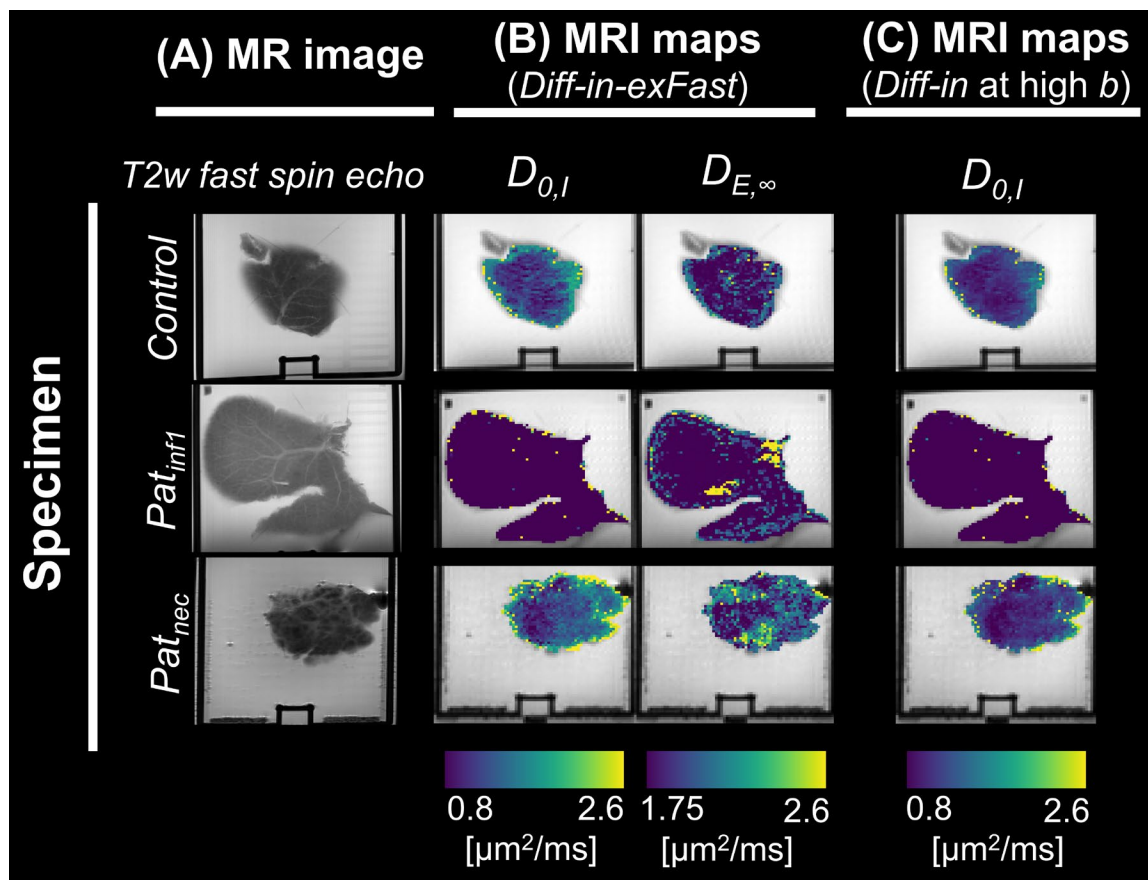


Fig. S10: diffusivity metrics from biophysical MRI models in fixed *ex vivo* mouse livers.

(A): high-resolution fast spin echo scan acquired in fixed mouse livers scanned *ex vivo* on the 9.4T Bruker system. **(B):** diffusivity metrics from biophysical model *Diff-in-exFast*, namely: intrinsic intra-cellular cytosolic diffusivity $D_{0,I}$; asymptotic extra-cellular diffusion coefficient $D_{E,\infty}$. **(C):** intrinsic intra-cellular cytosolic diffusivity $D_{0,I}$ from model *Diff-in* fitted to high b-value images ($b > 1800 \text{ s/mm}^2$). Maps from 3 specimens are reported along different rows. The specimens are representative of the 3 different microstructural phenotypes seen in our mouse liver data. From top to bottom, these are: normal liver structures (illustrated by the *Control* case, e.g., mouse with no biopsy implantation); pathology following biopsy implantation, consisting of an immature, lympho-proliferative process (infiltration of small cells in sinusoidal spaces, illustrated by case *Pat_{inf1}*); pathology following biopsy implantation, consisting of extended necrosis and inflammation (illustrated by case *Pat_{nec}*).

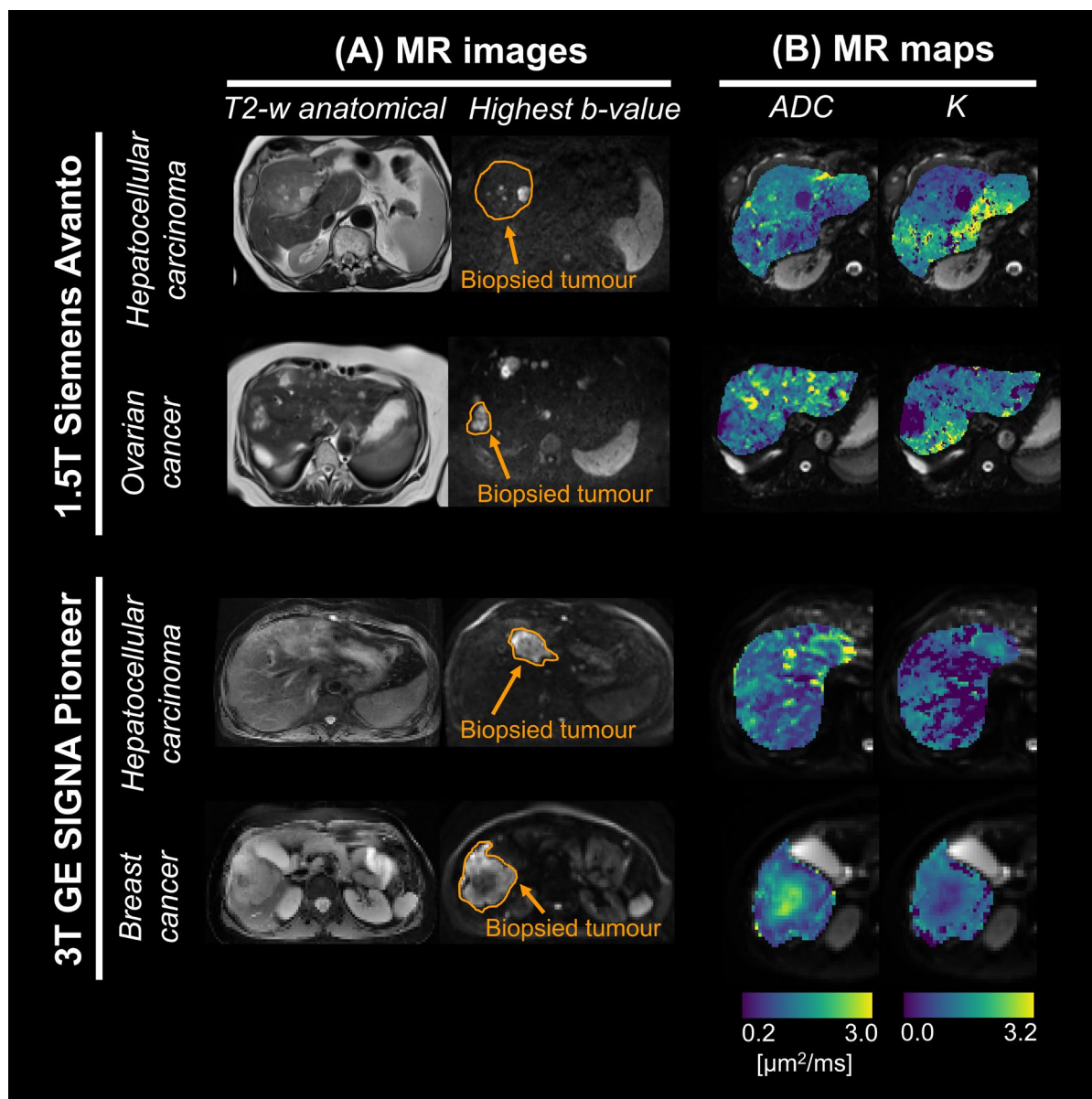


Fig. S11: standard diffusion MRI metrics in patients *in vivo*.

(A): high-resolution fast spin echo scan as well as a high b-value diffusion image, with biopsied tumour outlined. (B): standard diffusion metrics in the biopsied tumour. Metrics are: apparent diffusion coefficient (ADC) and apparent diffusion kurtosis excess (K). These were obtained by fitting the standard diffusion kurtosis signal representation $s = s_0 \exp(-b ADC + K (b ADC)^2/6)$ to the set of measurements at fixed, minimum TE and $b > 100$ s/mm². Maps are shown in four representative patients (two patients for each MRI scanner), along different rows. For the 1.5T Siemens scanner (first and second rows from top): patient 6 (primary hepatocellular carcinoma) and patient 3 (liver metastases from ovarian cancer). For the 3T GE scanner (third and fourth rows from top): patient 24 (primary hepatocellular carcinoma) and patient 30 (liver metastases from breast cancer).

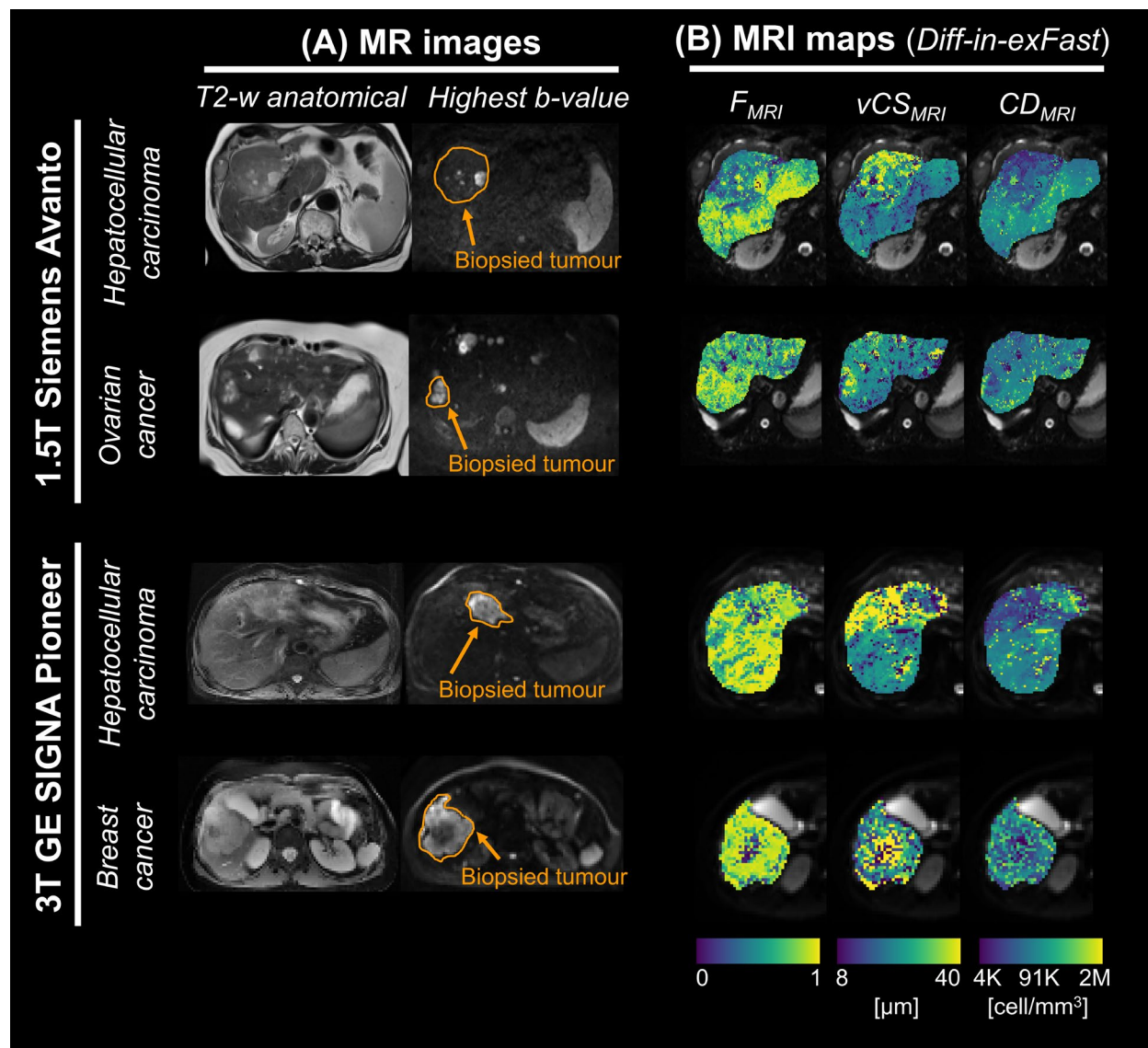


Fig. S12: key parametric maps of the *Diff-in-exFast* model in patients *in vivo*.

(A): high-resolution fast spin echo scan as well as a high b-value diffusion image, with biopsied tumour outlined. (B): salient metrics of the *Diff-in-exFast* model fitted to the whole set of images with negligible vascular signal contributions ($b > 100$ s/mm²). Metrics are shown in the biopsied tumour. From left to right: intra-cellular signal fraction F_{MRI} ; volume-weighted cell size index vCS_{MRI} index; cell density per unit volume CD_{MRI} . Metrics are shown in four representative patients (two patients for each MRI scanner), along different rows. For the 1.5T Siemens scanner (first and second rows from top): patient 6 (primary hepatocellular carcinoma) and patient 3 (liver metastases from ovarian cancer). For the 3T GE scanner (first and second rows from bottom): patient 24 (primary hepatocellular carcinoma) and patient 30 (liver metastases from breast cancer).

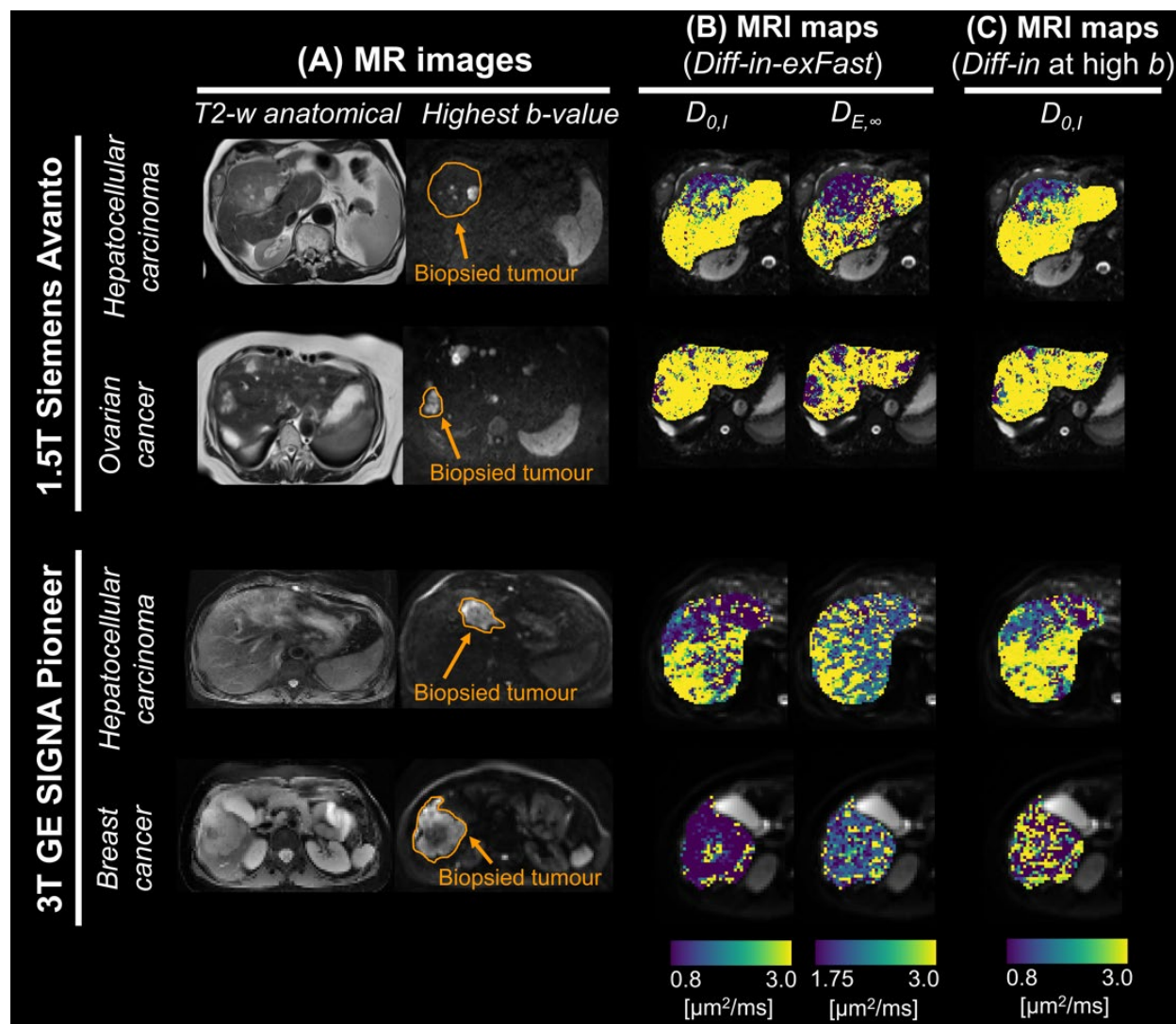


Fig. S13: diffusivity metrics from biophysical MRI models in patients *in vivo*.

(A): high-resolution fast spin echo scan as well as a high b-value diffusion image, with biopsied tumour outlined. (B): diffusivity maps from biophysical model *Diff-in-exFast* in the biopsied tumour. Metrics are: intra-cellular cytosolic diffusivity $D_{0,l}$ and asymptotic extra-cellular diffusion coefficient $D_{E,\infty}$. (C): intra-cellular cytosolic diffusivity $D_{0,l}$ for biophysical model *Diff-in* fitted being fitted only to high b-value images ($b > 900$ s/mm²). Metrics are shown in four representative patients (two patients for each MRI scanner), along different rows. For the 1.5T Siemens scanner (first and second rows from top): patient 6 (primary hepatocellular carcinoma) and patient 3 (liver metastases from ovarian cancer). For the 3T GE scanner (first and second rows from bottom): patient 24 (primary hepatocellular carcinoma) and patient 30 (liver metastases from breast cancer).

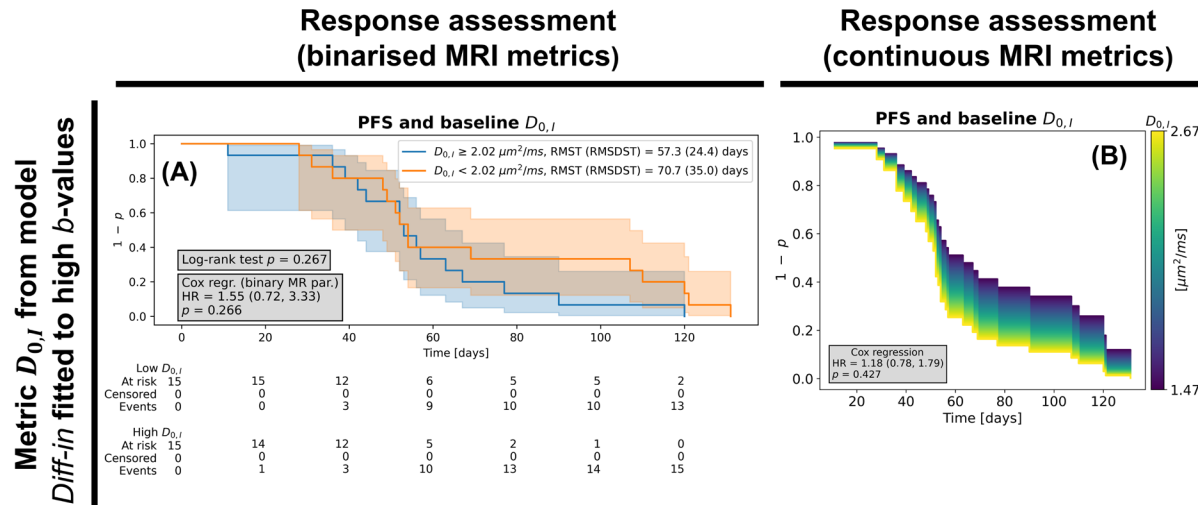


Fig. S14: immunotherapy response assessment based on *Diff-in* cytosol diffusivity estimates.

This figure reports on the dependence of patients' progression-free survival (PFS) on the average value of the intrinsic intra-cellular cytosol diffusivity $D_{0,I}$ within liver tumours at baseline (i.e., before starting immunotherapy), as obtained by fitting model *Diff-in* at high b-value. Left (panel A): Kaplan-Meier (KM) survival curves of two groups obtained by splitting patients based on baseline $D_{0,I}$ (lower or higher than the sample median). The grey panel reports the p-values of a log-rank sum test comparing the KM curves, and of a Cox regression based on the binarised MRI metric (with the corresponding hazard ratio (HR) estimate and 95% confidence interval). The legend reports the Restricted Mean Survival Time (RMST) and Restricted Standard Deviation of Survival Time (RSDST) for each KM curve. Right (panel B): results from univariate Cox regression where the baseline $D_{0,I}$ is a continuous predictor of the survival. The panel shows how changes in baseline $D_{0,I}$ modulate the survival curve, given the HR estimated for each metric. In the grey box, the p-value and HR (with 95% CI) corresponding to the baseline MRI metric are reported. In all panels, the y-axis shows $1 - p$, with p being the probability of progression, while the x-axis shows the time to progression (in days).

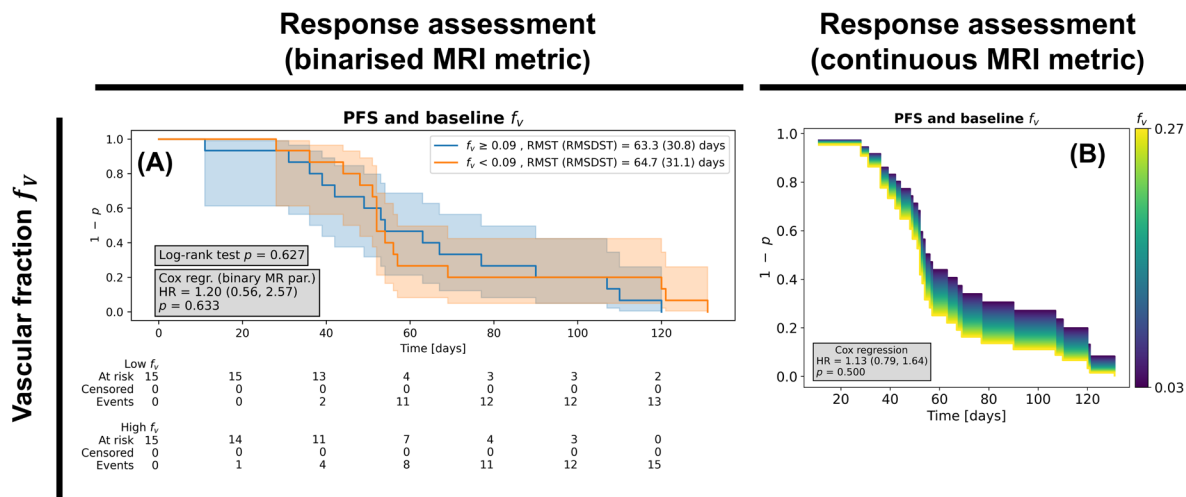


Fig. S15: immunotherapy response assessment based on vascular fraction estimates.

This figure reports on the dependence of patients' progression-free survival (PFS) on the average value of the vascular signal fraction f_v within liver tumours at baseline (i.e., before starting immunotherapy). The vascular signal fraction f_v was computed in the initial fitting step, which disentangles the vascular from the non-vascular (tissue) signal, before the latter is split into intra-/extra-cellular contributions in the biophysical model fitting step. The same representation layout as in Fig. S6 was used. Left (A): Kaplan-Meier (KM) analysis, log-rank sum test and Cox regression based on the binarised f_v (higher/lower than the sample median). Right (B): Cox regression modelling the probability of survival as a continuous function of baseline f_v . In all panels, the y-axis shows $1 - p$, with p being the probability of progression, while the x-axis shows the time to progression (in days).

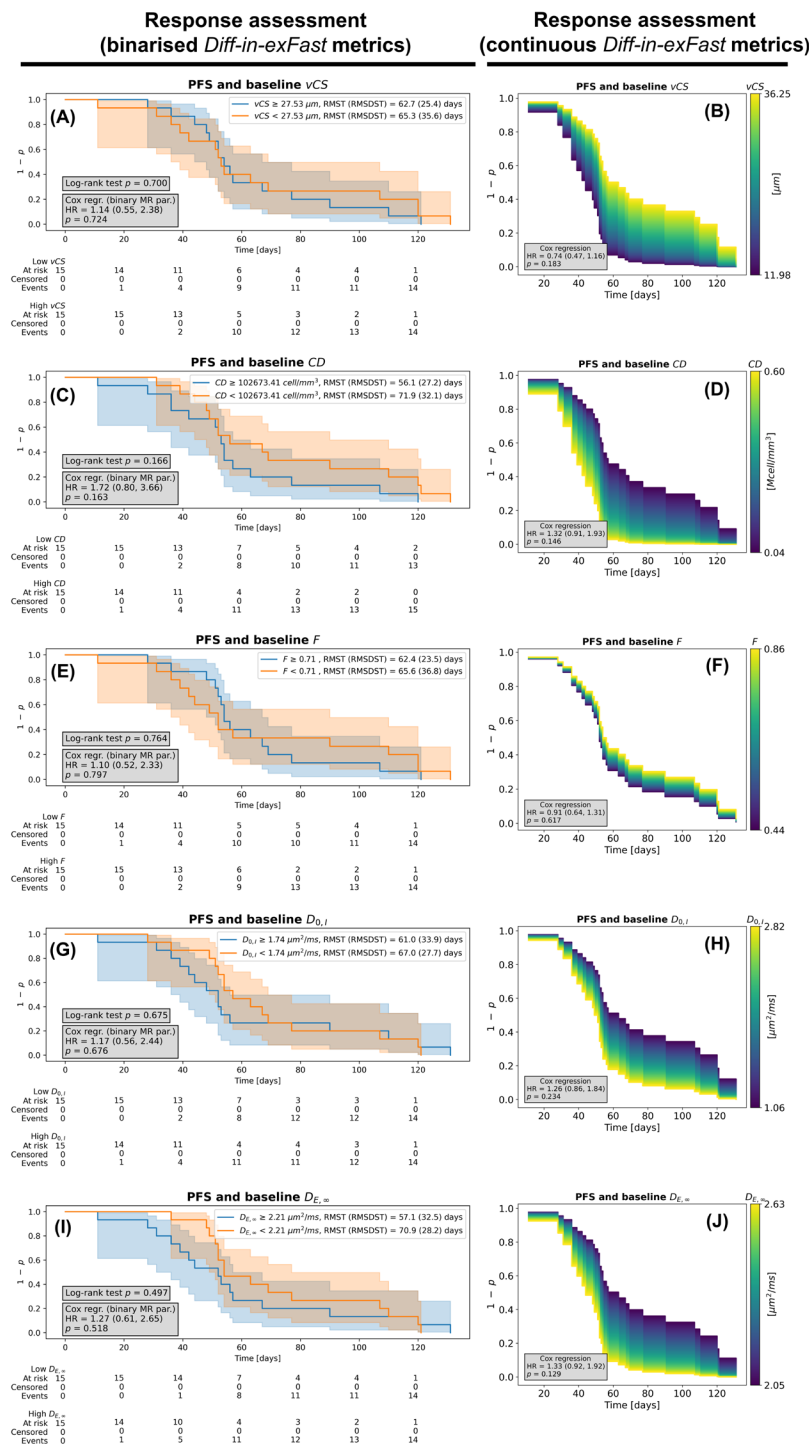


Fig. S16: immunotherapy response assessment based on *Diff-in-exFast* MRI metrics.

This figure reports on the dependence of patients' progression-free survival (PFS) on the average value of all *Diff-in-exFast* metrics within liver tumours at baseline (i.e., before starting immunotherapy). In each row, from top to bottom: PFS based on baseline volume-weighted Cell Size vCS (panels A and B), Cell Density CD (panels C and D), intra-cellular fraction F (panels E

and **F**), intrinsic intra-cellular cytosol diffusivity $D_{0,I}$ (panels **G** and **H**), asymptotic extra-cellular diffusion coefficient $D_{E,\infty}$ (panels **I** and **J**). The same representation layout as in Fig. S6 was used. Left (**A**, **C**, **E**, **G**, **I**): Kaplan-Meier (KM) analysis, log-rank sum test and Cox regression based on the binarised MRI metrics (higher/lower than the sample median). Right (**B**, **D**, **F**, **H**, **J**): Cox regression modelling the probability of survival as a continuous function of baseline MRI metrics. In all panels, the y-axis shows $1 - p$, with p being the probability of progression, while the x-axis shows the time to progression (in days).

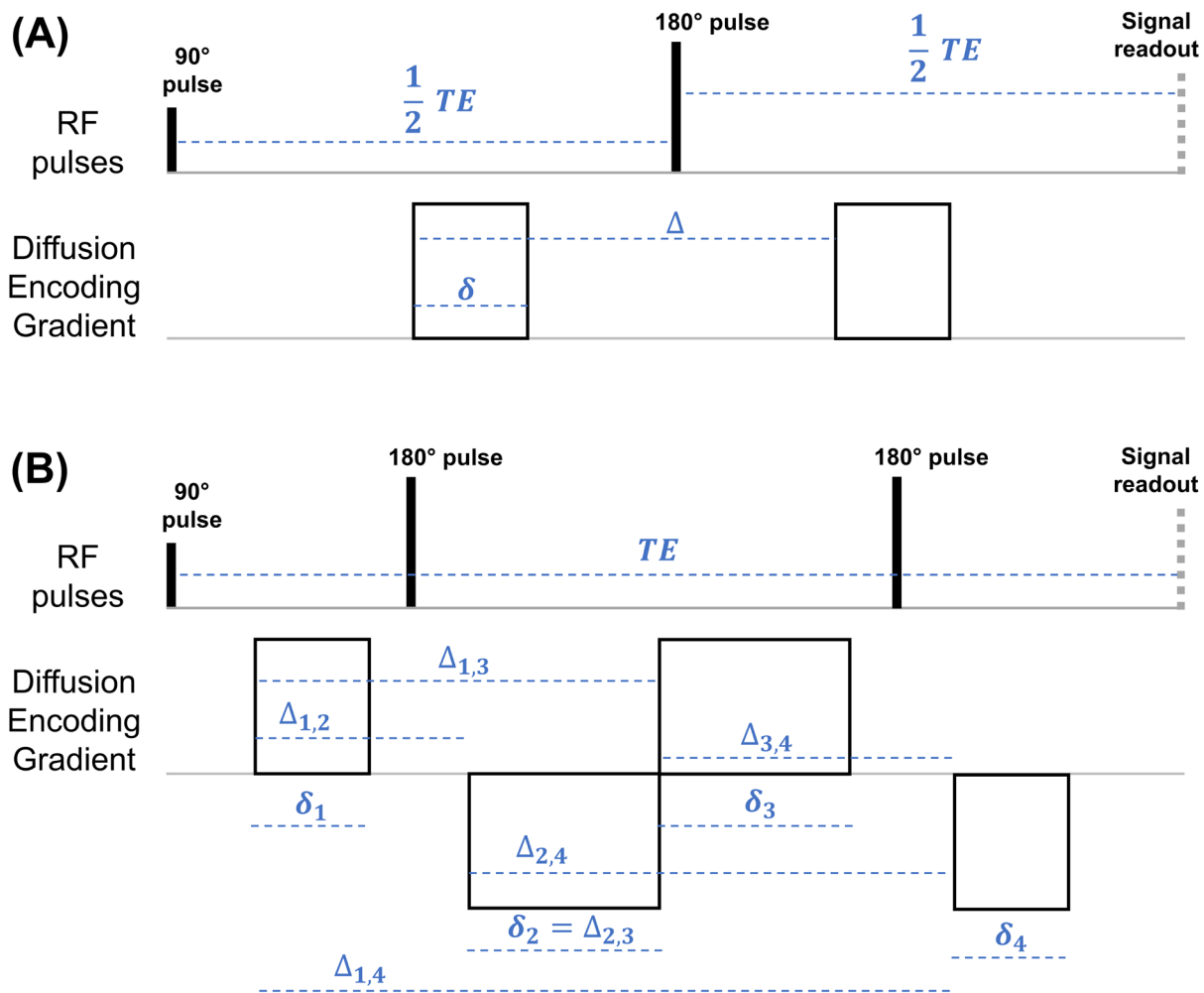


Fig. S17: schematic of the dMRI sequences used in this study.

(A): pulsed gradient spin echo (PGSE sequence, also known as Stejskal-Tanner sequence, pulsed-field gradient (PFG), or single linear diffusion encoding) used to acquire data on the 9.4T Bruker system on fixed mouse livers *ex vivo* and on the 3T GE system on patients *in vivo*. δ and Δ respectively indicate the diffusion gradient duration and separation, while TE is the echo time. (B): twice-refocussed diffusion-weighted spin echo sequence used to acquire data on the 1.5T Siemens system on patients *in vivo*. δ_n and $\Delta_{n,m}$ respectively indicate the duration of the n -th gradient lobe and the separation time between the n -th and m -th gradient lobes, for $n, m = 1, \dots, 4$. TE is again the echo time. In both panels, “Signal readout” corresponds to sampling the center of the k-space (i.e., zero spatial frequency).

Table S1: results of the model selection based on the Total Correlation Score (TCS) as obtained on simulated dMRI signals.

We performed model selection on synthetic signals simulated for all the dMRI protocols considered in this study (*ex vivo* PGSE, used on fixed mouse livers; *in vivo* PGSE and DW TRSE, used in patients *in vivo*; see Methods for a full description of the protocols). We fitted the models on protocol subsets obtained with the same b-value thresholds used when analysing actual MRI signals (“Regular fit”: fitting on all b-values with negligible vascular contributions; “High *b* only fit”: fitting on b-values minimising extra-cellular signal contributions). The Table reports the value of $TCS = r(vCS_{est}, vCS_{gt}) + r(F_{est}, F_{gt})$, where vCS is the cell size, F the intra-cellular fraction, $r(x, y)$ the Pearson’s correlation between variables x and y computed pooling together all synthetic voxels, and where subscripts *est* and *gt* respectively indicate estimated and ground truth values. Higher values of TCS point towards better model performance. For each protocol and fitting strategy, the model with the highest TCS is flagged by gray shadowing and bold font.

Model	Protocol: <i>ex vivo</i>		Protocol: <i>in vivo</i> PGSE		Protocol: <i>in vivo</i> TRSE	
	Regular fit	High <i>b</i> only fit	Regular fit	High <i>b</i> only fit	Regular fit	High <i>b</i> only fit
	<i>Diff-in-exTD</i>	0.217	-0.111	0.312	0.202	0.604
<i>Diff-in-ex</i>	0.406	0.089	0.472	0.335	0.700	0.550
<i>Diff-in-exTDFast</i>	0.948	0.827	0.536	0.336	0.618	0.544
<i>Diff-in-exFast</i>	0.952	0.850	0.563	0.349	0.626	0.547
<i>Diff-in</i>	1.222	0.977	0.773	0.462	0.543	0.630

Table S2: results of the model selection based on the Histology Fidelity Criterion (HFC) as obtained on simulated dMRI signals.

We performed model selection on synthetic signals simulated for all the dMRI protocols considered in this study (*ex vivo* PGSE, used on fixed mouse livers; *in vivo* PGSE and DW TRSE, used in patients *in vivo*; see Methods for a full description of the protocols). We fitted the models on protocol subsets obtained with the same b-value thresholds used when analysing actual MRI signals (“Regular fit”: fitting on all b-values with negligible vascular contributions; “High *b* only fit”: fitting on b-values minimising extra-cellular signal contributions). For each model, the table reports the percentage of synthetic voxels where $HFC = |vCS_{est} - vCS_{gt}|/vCS_{gt} + |F_{est} - F_{gt}|/F_{gt}$ was the lowest across all models. Above, vCS is the cell size, F the intra-cellular fraction, and subscripts *est* and *gt* respectively indicate estimated and ground truth values. Higher percentages indicate smaller estimation errors, and therefore point towards better model performance. For each protocol and fitting strategy, the model with the highest proportion of synthetic voxels with minimum HFC is flagged by gray shadowing and bold font.

	Protocol: <i>ex vivo</i>		Protocol: <i>in vivo</i> PGSE		Protocol: <i>in vivo</i> TRSE	
	Regular fit	High <i>b</i> only fit	Regular fit	High <i>b</i> only fit	Regular fit	High <i>b</i> only fit
	Model					
<i>Diff-in-exTD</i>	12.62%	13.56%	21.69%	22.10%	26.69%	20.69%
<i>Diff-in-ex</i>	21.19%	16.62%	25.94%	20.35%	28.94%	24.31%
<i>Diff-in-exTDFast</i>	15.50%	14.94%	10.75%	12.27%	19.69%	14.69%
<i>Diff-in-exFast</i>	21.81%	10.50%	22.25%	11.33%	19.12%	12.12%
<i>Diff-in</i>	28.88%	44.38%	19.38%	33.94%	5.56%	28.19%

Table S3: results of the model selection based on the Bayesian Information Criterion (BIC) as obtained on simulated dMRI signals.

We performed model selection on synthetic signals simulated for all the dMRI protocols considered in this study (*ex vivo* PGSE, used on fixed mouse livers; *in vivo* PGSE and DW TRSE, used in patients *in vivo*; see Methods for a full description of the protocols). We fitted the models on protocol subsets obtained with the same b-value thresholds used when analysing actual MRI signals (“Regular fit”: fitting on all b-values with negligible vascular contributions; “High *b* only fit”: fitting on b-values minimising extra-cellular signal contributions). For each model, the table reports the percentage of synthetic voxels where the Bayesian Information Criterion (BIC, a standard metric of model fitting quality that penalises model complexity) was the lowest across all models. Higher percentages indicate smaller BIC values across synthetic voxels, and therefore point towards better model fitting quality. For each protocol and fitting strategy, the model with the highest proportion of synthetic voxels with minimum HFC is flagged by gray shadowing and bold font.

Model	Protocol: <i>ex vivo</i>		Protocol: <i>in vivo</i> PGSE		Protocol: <i>in vivo</i> TRSE	
	Regular fit	High <i>b</i> only fit	Regular fit	High <i>b</i> only fit	Regular fit	High <i>b</i> only fit
	<i>Diff-in-exTD</i>	0.12%	0.00%	0.00%	0.19%	0.00%
<i>Diff-in-ex</i>	31.25%	15.88%	17.44%	4.69%	40.69%	13.69%
<i>Diff-in-exTDFast</i>	0.00%	0.00%	0.00%	0.00%	0.00%	0.00%
<i>Diff-in-exFast</i>	3.44%	0.06%	6.69%	0.00%	21.38%	1.06%
<i>Diff-in</i>	65.19%	84.06%	75.88%	95.12%	38.00%	85.25%

Table S4: descriptive statistics of histology and MRI metrics in the fixed mouse livers.

The table reports mean and standard deviation (within brackets) of histology and dMRI metrics in the 7 fixed mouse livers that were scanned on a 9.4T Bruker system. Histological maps were computed within patches matching the in-plane MRI resolution and then warped non-linearly to dMRI space. The histological maps are: per-patch intra-cellular area fraction F_{histo} , per-patch arithmetic mean cell size aCS_{histo} ; per-patch volume-weighted mean cell size vCS_{histo} , cell density per unit patch area CD_{histo} . dMRI metrics are: apparent diffusion coefficient ADC , apparent diffusion kurtosis excess K , intra-cellular signal fraction F_{MRI} , volume-weighted cell size index vCS_{MRI} , apparent cell density per unit volume CD_{MRI} . Metrics F_{MRI} , vCS_{MRI} and CD_{MRI} are reported for both models *Diff-in-exFast* and model *Diff-in*, with *Diff-in* fitted only to high b-value images ($b > 1800$ s/mm²). In model *Diff-in-exFast*, the extra-cellular ADC does not feature diffusion time dependence and is constrained to be larger than the intra-cellular ADC. In model *Diff-in*, the extra-cellular signal is modelled as negligible compared to the intra-cellular one (i.e., total signal dominated by intra-cellular water). Specimens are: *Control* (normal liver structures); *NA1* and *NA2* (normal appearing cases, i.e., normal liver structures despite sub-cutaneous biopsy implantation); *Pat_{infl-3}* (cases developing liver pathology following sub-cutaneous biopsy implantation, consisting of small cell infiltration in sinusoidal spaces, in between larger hepatocytes); *Pat_{nec}* (case developing liver pathology following sub-cutaneous biopsy implantation, consisting of necrosis and inflammation). aCS_{histo} , always considerably lower than vCS_{histo} , was included to highlight the impact of the largest cells in the computation of statistics based on weighting by cell volume (vCS_{histo}).

Specimen	Histology				Standard diffusion metrics		<i>Diff-in-exFast</i> model			<i>Diff-in</i> model at high b		
	F_{histo}	aCS_{histo} [μm]	vCS_{histo} [μm]	$CD_{histo}/10^2$ [cell/mm ²]	ADC [$\mu\text{m}^2/\text{ms}$]	K	F_{MRI}	vCS_{MRI} [μm]	$CD_{MRI}/10^5$ [cell/mm ³]	F_{MRI}	vCS_{MRI} [μm]	$CD_{MRI}/10^5$ [cell/mm ³]
<i>Control</i>	0.75 (0.18)	21.63 (1.85)	27.1 (1.6)	3.2 (1.1)	1.50 (0.32)	0.33 (0.20)	0.60 (0.18)	33.2 (5.7)	0.38 (1.69)	0.56 (0.11)	36.5 (5.1)	0.28 (1.44)
<i>NA1</i>	0.59 (0.25)	23.97 (3.05)	27.8 (3.2)	2.1 (1.1)	1.61 (0.37)	0.10 (0.15)	0.66 (0.25)	30.5 (8.4)	0.69 (2.18)	0.54 (0.16)	32.2 (7.5)	0.45 (1.68)
<i>NA2</i>	0.76 (0.14)	23.46 (1.41)	29.4 (1.2)	2.7 (0.7)	1.43 (0.44)	0.51 (0.29)	0.80 (0.16)	22.2 (4.8)	1.01 (1.35)	0.71 (0.12)	22.8 (5.0)	0.83 (1.15)
<i>Pat_{infl1}</i>	0.80 (0.20)	15.73 (2.18)	20.8 (2.7)	6.7 (2.2)	0.58 (0.41)	0.98 (0.49)	0.83 (0.13)	13.4 (3.1)	4.20 (2.22)	0.77 (0.14)	12.4 (3.0)	4.86 (2.27)
<i>Pat_{infl2}</i>	0.79 (0.20)	21.41 (2.29)	26.8 (2.7)	3.5 (1.2)	1.67 (0.39)	0.17 (0.17)	0.37 (0.22)	31.2 (7.5)	0.44 (2.06)	0.41 (0.14)	37.1 (6.0)	0.30 (1.57)
<i>Pat_{infl3}</i>	0.70 (0.27)	20.95 (1.75)	27.6 (1.7)	3.1 (1.3)	1.57 (0.62)	0.43 (0.31)	0.63 (0.23)	23.6 (8.8)	1.27 (2.62)	0.59 (0.20)	24.2 (8.0)	0.97 (2.01)
<i>Pat_{nec}</i>	0.52 (0.25)	19.10 (3.33)	25.9 (2.8)	3.4 (2.3)	1.49 (0.44)	0.31 (0.22)	0.61 (0.23)	28.2 (6.6)	0.58 (1.93)	0.54 (0.16)	31.6 (6.7)	0.42 (1.66)

Table S5. Hazard ratios obtained from Cox regression models controlling for sex, age, and baseline tumour volume.

The table reports the Hazard Ratios (HR) for different MRI metrics, with relative 95% confidence interval and p-value, estimated through Cox proportional hazard regressions. The models assessed the dependence of the probability of progression on the baseline mean value of MRI metrics within liver tumours, accounting for sex, age and tumour volume. Results are shown for standard diffusion metrics (apparent diffusion and excess kurtosis coefficients, ADC and K), for the vascular signal fraction f_v , for metrics from model *Diff-in-exFast* (intra-cellular fraction F , volume-weighted cell size vCS , cell density per unit volume CD , intrinsic intra-cellular cytosolic diffusivity $D_{0,I}$, extra-cellular asymptotic diffusion coefficient $D_{E,\infty}$) and for metrics from model *Diff-in* (intra-cellular fraction F , volume-weighted cell size vCS , cell density per unit volume CD , intrinsic intra-cellular cytosolic diffusivity $D_{0,I}$) fitted at high b-value ($b > 900$ s/mm²). Grey shadowing highlights HRs whose p-value is ≤ 0.05 .

	HR of MRI metric	HR of male sex	HR of age	HR of tumour volume
Standard diffusion MRI metrics				
ADC	1.00 (0.67; 1.49); $p = 1.00$	0.71 (0.32; 1.55); $p = 0.39$	0.97 (0.94; 0.99); $p = 0.02$	0.32 (0.06; 1.70); $p = 0.18$
K	1.36 (0.94; 1.97); $p = 0.11$	0.64 (0.29; 1.41); $p = 0.27$	0.97 (0.94; 1.00); $p = 0.02$	0.35 (0.08; 1.54); $p = 0.17$
Other metrics (from vascular vs non-vascular fitting initialisation step)				
f_v	1.16 (0.79; 1.71); $p = 0.44$	0.77 (0.35; 1.68); $p = 0.51$	0.96 (0.93; 0.99); $p = 0.01$	0.34 (0.17; 2.56); $p = 0.17$
Metrics from MRI model <i>Diff-in-exFast</i>				
F	0.87 (0.61; 1.26); $p = 0.46$	0.78 (0.35; 1.72); $p = 0.54$	0.97 (0.94; 1.00); $p = 0.02$	0.31 (0.06; 1.58); $p = 0.16$
vCS	0.70 (0.44; 1.12); $p = 0.14$	0.78 (0.36; 1.68); $p = 0.53$	0.97 (0.94; 0.99); $p = 0.02$	0.35 (0.08; 1.46); $p = 0.15$
CD	1.53 (1.00; 2.34); $p = 0.05$	0.63 (0.29; 1.38); $p = 0.25$	0.96 (0.93; 0.99); $p = 0.01$	0.32 (0.06; 1.81); $p = 0.20$
$D_{0,I}$	1.45 (0.98; 2.14); $p = 0.06$	0.68 (0.31; 1.47); $p = 0.33$	0.96 (0.93; 0.99); $p = 0.01$	0.36 (0.09; 1.35); $p = 0.13$
$D_{E,\infty}$	1.41 (0.97; 2.05); $p = 0.07$	0.69 (0.32; 1.48); $p = 0.34$	0.96 (0.94; 0.99); $p = 0.01$	0.40 (0.13; 1.26); $p = 0.12$
Metrics from MRI model <i>Diff-in</i> fitted to high b-value images				
F	0.79 (0.54; 1.17); $p = 0.24$	0.80 (0.36; 1.74); $p = 0.57$	0.97 (0.94; 0.99); $p = 0.02$	0.33 (0.07; 1.49); $p = 0.15$
vCS	0.59 (0.37; 0.93); $p = 0.02$	0.66 (0.30; 1.43); $p = 0.29$	0.96 (0.94; 0.99); $p = 0.01$	0.40 (0.12; 1.37); $p = 0.14$
CD	1.65 (1.12; 2.44); $p = 0.01$	0.61 (0.28; 1.35); $p = 0.22$	0.96 (0.93; 0.99); $p = 0.01$	0.36 (0.09; 1.52); $p = 0.17$
$D_{0,I}$	1.28 (0.82; 1.98); $p = 0.28$	0.67 (0.31; 1.45); $p = 0.31$	0.96 (0.94; 0.99); $p = 0.01$	0.37 (0.09; 1.48); $p = 0.16$

